

# Photolysis of Cometary Organic Dust Analogs on the EXPOSE-R2 Mission at the International Space Station

G.A. Baratta,<sup>1</sup> M. Accolla,<sup>1</sup> D. Chaput,<sup>2</sup> H. Cottin,<sup>3</sup> M.E. Palumbo,<sup>1</sup> and G. Strazzulla<sup>1</sup>

## Abstract

We describe the results obtained on a set of organic samples that have been part of the experiment “Photochemistry on the Space Station (PSS)” on the EXPOSE-R2 mission conducted on the EXPOSE-R facility situated outside the International Space Station (ISS). The organic samples were prepared in the Catania laboratory by 200 keV He<sup>+</sup> irradiation of N<sub>2</sub>:CH<sub>4</sub>:CO icy mixtures deposited at 17 K, on vacuum UV (VUV) transparent MgF<sub>2</sub> windows. This organic material contains different chemical groups, including triple CN bonds, that are thought to be of interest for astrobiology. It is widely accepted that materials similar to that produced in the laboratory by ion irradiation of frozen ices could be present in some astrophysical environments such as comets. Once expelled from comets, these materials are exposed to solar radiation during their interplanetary journey. In the young Solar System, some of these processed materials could have reached early Earth and contributed to its chemical and prebiotic evolution. The samples were exposed for 16 months to the unshielded solar UV photons. It was found that, if an interplanetary dust particle (IDP) containing organic material (50% vol) is large enough (>20–30 μm), relevant chemical groups, such as those containing the CN triple bond, can survive for many years (>10<sup>4</sup> years) in the interplanetary medium. Key Words: Astrobiology—Astrochemistry—Comets—International Space Station—Photochemistry—Infrared spectroscopy. Astrobiology 19, 1018–1036.

## 1. Introduction

SOLAR UV RADIATION is fundamental to organic chemistry and indeed drives most chemical evolution processes, via photochemical reactions, in the Solar System (Cottin *et al.*, 2015). In recent years, many experimental studies have been conducted with the intent to discern the effects of cosmic UV photons on organics in different astrophysical environments. These studies have used varying sources that emit photons in the range of 100 nm < λ < 200 nm. It should be noted, however, that none of these sources have the capability to accurately reproduce the full solar UV spectrum (Cottin *et al.*, 2015a, 2015b, 2017). In particular, differences as large as a factor >100 in the photolysis kinetic can be found between the extrapolation of laboratory results to space conditions and measurements of organic samples exposed to low Earth orbit conditions (Guan *et al.*, 2010). Earth’s atmosphere blocks all ionizing (λ < 125 nm) and most of the harmful (λ < 310 nm) UV solar photons. The International Space Station (ISS) offers the unique opportunity to expose, for relatively long

periods of time, samples to the real, unfiltered solar electromagnetic spectrum. Here, we present results obtained from a set of organic samples that were part of the Photochemistry on the Space Station (PSS) experiment on the EXPOSE-R2 mission (Cottin *et al.*, 2015b, Rabbow *et al.*, 2017). The EXPOSE-R2 mission used the ESA EXPOSE-R facility, which is situated outside the ISS on the URIM-D platform of the Russian module Zvezda. EXPOSE-R accommodated three European astrobiological experiments (BIOMEX, BOSS, PSS) and one Russian (BIODIVERSITY) astrobiological experiment, all of which comprised several chemical and biological samples that were exposed to cosmic ionizing radiation and solar UV photons.

Our organic residues were prepared by 200 keV He<sup>+</sup> irradiation of frozen N<sub>2</sub>:CH<sub>4</sub>:CO ice mixtures deposited, at 17 K, on MgF<sub>2</sub> vacuum UV (VUV) transparent substrates. It is generally understood that materials similar to those produced by energetic processing of ices may be present in some astrophysical environments such as interstellar grains (Pendleton and Allamandola, 2002).

<sup>1</sup>INAF - Osservatorio Astrofisico di Catania, Catania, Italy.

<sup>2</sup>Centre National d’Etudes Spatiales (CNES), Centre Spatial de Toulouse, Toulouse, France.

<sup>3</sup>Laboratoire Interuniversitaire des Systèmes Atmosphériques (LISA), UMR CNRS 7583, Université Paris Est Créteil et Université Paris Diderot, Institut Pierre Simon Laplace, Créteil, France.

We chose an ice mixture that well represents ices that occur at the surface of trans-neptunian objects (TNOs) and comets in the Oort cloud. Indeed, the spectral signatures of solid nitrogen, methane, and carbon monoxide are seen in TNOs (*e.g.*, Pluto; see Protopapa *et al.*, 2017). Furthermore, a number of studies have obtained evidence of dark organic materials that may have been produced by cosmic ion irradiation of TNO surface ices (*e.g.*, Grundy and Buie, 2002; Brunetto *et al.*, 2006). The N<sub>2</sub>:CH<sub>4</sub>:CO ice mixture we used in our study is also representative of comets in the Oort cloud. It has been proposed that, as a consequence of galactic cosmic ray (GCR) irradiation, a refractory crust, under which water ice is the dominant species, occurs on comets in the Oort cloud (Strazzulla and Johnson, 1991). In particular, the formation of a stable crust, due to the conversion of low-molecular-weight hydrocarbons into a stable organic residue, requires an irradiation dose on the order of 100 eV/16u (Strazzulla and Johnson, 1991). Owing to the solar modulation, maximum irradiation doses are reached far from the Sun in the local interstellar medium (Cooper *et al.*, 2003). For comets in the Oort cloud, 100 eV/16u have penetrated to a depth of 1–2 m throughout the age of the Solar System. Lower doses of 30 eV/16u penetrate to a significantly greater depth of 5–10 m, (see Fig. 12 of Strazzulla and Johnson, 1991). Thanks to Rosetta measurements, a complex macromolecular material has been detected in comet 67P. In particular, it was found that 50% in mass of dust particles ejected from the nucleus of the comet are composed of this organic material (Fray *et al.*, 2016; Bardyn *et al.*, 2017). When a comet from the Oort cloud or from the Kuiper belt (*i.e.*, the TNOs' region) enters the inner Solar System, the water ice-dominated sublimation at ~3 AU (astronomical units) or the sublimation of other more volatile species such as CO, CO<sub>2</sub>, N<sub>2</sub>, CH<sub>4</sub> at much longer heliocentric distance (up to ~25 AU; see Szabó *et al.*, 2011) ejects gas and dust. Cometary dust constitutes a fraction of those interplanetary dust particles (IDPs) that have been collected in Earth's atmosphere by airborne impacting collectors flown at an altitude of 18–20 km and of those micrometeorites collected in Antarctica. The remaining fraction of IDPs and of the micrometeorites come from asteroids (Genge *et al.*, 2008). The ultracarbonaceous Antarctic micrometeorites (UCAMMs) constitute a particular class of micrometeorites (Dobrica *et al.*, 2009, 2012; Dartois *et al.*, 2013, 2018). It has been shown that UCAMMs have a carbonaceous phase with IR signatures similar to those of the organic residues described in this work (Baratta *et al.*, 2015). It is believed that these high-carbon-content (> 50% vol) and high-N/C-ratio (*e.g.*, 0.12 in DC65) micrometeorites originated in the outer Solar System beyond the nitrogen snow-line, for example in an Oort cloud comet by cosmic ray irradiation (Dartois *et al.*, 2013, 2018). In general, the origin of organic materials present in IDPs and micrometeorites is still under debate, though various processes may be a contributing factor, such as UV photolysis, cosmic ion irradiation, and grain-surface chemistry, all of which may act at different evolutionary phases. Comets accreted in the cold outer regions of the protoplanetary disk and hence cometary materials may have preserved those original components which formed the Solar System (Sandford *et al.*, 2008). Hence, UV- and GCR-processed interstellar grains could have been incorporated into comets. It is important to note that hot spots in some IDPs have a D/H ratio that reaches the

value of interstellar molecules, which suggests that interstellar molecular-cloud organic materials from the early Solar System may have survived (Messenger, 2000). Organic matter in IDPs and micrometeorites could also have originated in the protoplanetary disk. In the cold part of the disk, in particular, ices would have covered small (from sub-micrometer to millimeter) refractory grains. During this early phase, the icy mantles would have received large amounts of energy from cosmic rays, solar particles, and UV photons that could have transformed a fraction of the ice into organics (Dartois *et al.*, 2013). In particular, it has been found that icy grains that originated in the outer disk ( $T < 30$  K) experienced UV irradiation exposures and thermal warming similar to those that have been shown to produce complex organics in laboratory experiments (Ciesla and Sandford, 2012). Carbonaceous matter that formed in these small grains could then have been incorporated into icy proto-/cometary objects and eventually delivered to the inner Solar System by comets. Hence, IDPs and micrometeorites could contain materials similar to the PSS organic residues if emitted from the external (ion-processed) layers of a comet or as a heritage of irradiation that occurred in the protoplanetary disk phase. During their journey in the interplanetary medium, these materials would have been exposed to GCRs, solar UV photons, and the solar ion population before reaching Earth or other objects in the Solar System. Hence, materials similar to those discussed here could have reached prebiotic Earth. As is shown in the next sections, the organic residues we have produced contain astrobiologically relevant species such as nitriles (Palumbo *et al.*, 2000a, 2000b; Kaiser and Balucani, 2001). One of the key points for the synthesis of the first biomonomers is the availability of suitable precursor organics under primitive Earth conditions. According to Ruiz-Mirazo *et al.* (2014), the role of extraterrestrial organics in providing precursor materials was significant. The aim of the present study was to analyze the destruction/modification, induced in space by solar UV photons, of the relevant chemical species contained in the organic residue.

## 2. Materials and Methods

### 2.1. Sample preparation and characterization

Sample preparation and characterization was described previously in the work of Baratta *et al.* (2015), to which the reader is referred for further details. Here, we offer a brief description of the procedures and experimental setup that was adopted to prepare and characterize the samples. A schematic view of the experimental apparatus can be seen in Fig. 1a.

The experimental apparatus used to irradiate frozen ices consists of a stainless steel ultrahigh vacuum (UHV) chamber with a base pressure lower than  $10^{-9}$  mbar. Gas mixtures are prepared in a separate mixing chamber that is pre-evacuated to a pressure of  $\sim 10^{-7}$  mbar by using a turbomolecular pump. Once prepared, the gas mixture is admitted through a flow-regulated valve in the UHV main chamber, where it freezes on an IR transparent substrate that is placed in thermal contact with the tail section of a closed-cycle CTI helium cryostat ( $T = 16$ – $300$  K). The thickness and refractive index of the deposited ices can be measured, during accretion, by looking at the interference pattern (intensity versus time) given by a He-Ne laser beam ( $\lambda = 543.5$  nm) reflected

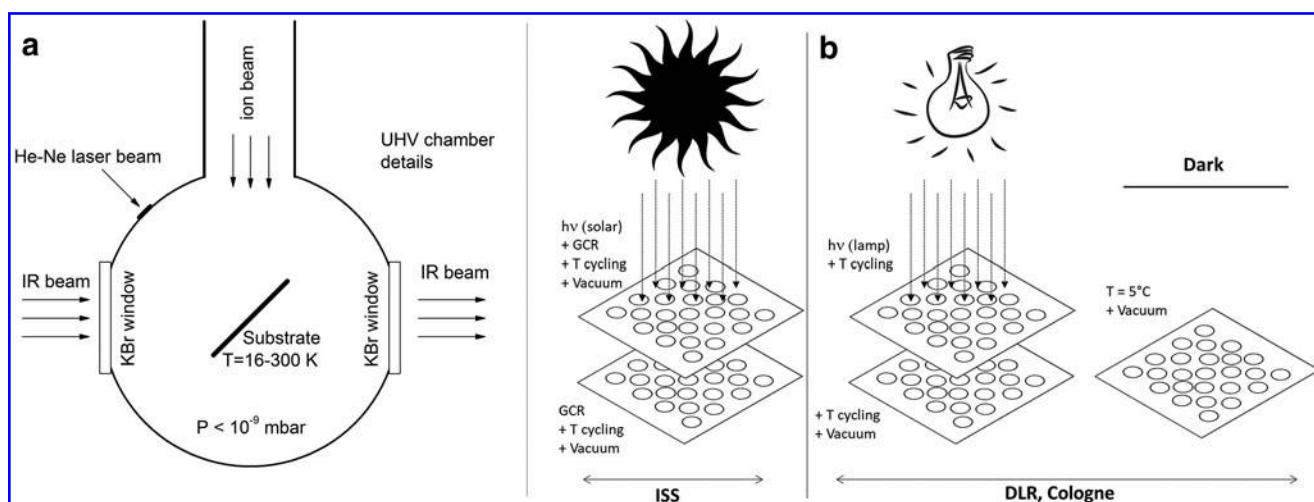


**FIG. 1.** (a) Schematic view of the experimental apparatus used to produce the organic residues. (b) Scheme showing the experimental breakdown of samples between the ISS and DLR Cologne, and the environmental conditions to which they have been exposed.

at near-normal incidence ( $i=2.9^\circ$ ) by the ice-vacuum and ice-substrate interfaces (see Urso *et al.*, 2016, and references therein).

Fast ions, up to an energy of 200 keV (400 keV for double ionization), are obtained by a 200 kV Danfysik implanter. The ion beam is electrostatically swept over the substrate to obtain a uniform coverage of the irradiated ices. The total ion fluence found in different astrophysical scenarios can be easily reproduced in the laboratory. Nevertheless, it should be noted that this occurs on very different timescales. In general, since it is impossible to reproduce, in the laboratory, the dose rate found in astrophysical scenarios and obtain measurable effects in human lifetime, the results cannot depend on the dose rate; any experimental result that depends on the dose rate, such as the beam-induced heating of the target, cannot be extrapolated to any astrophysical scenario. The ion beam current was kept below  $1 \mu\text{A}/\text{cm}^2$  to prevent a macroscopic heating of the frozen film. It should be noted that a temperature increase of 15 K would have caused the complete sublimation of CO and N<sub>2</sub> from the mixture. We have verified many times that the effects induced by fast ions on frozen mixtures do not depend on the dose rate for such low ion currents. In any case, the extrapolations of the laboratory results to astrophysical scenarios implicitly assume that other processes that could interfere with the cosmic ion processing (such as resurfacing and diffusion) do not take place on the astrophysical object. The ion fluence was measured by integrating the ion current monitored during irradiation. The irradiation dose was calculated by multiplying the ion fluence (ions/cm<sup>2</sup>) and the energy loss per unit path length (stopping power; eV cm<sup>2</sup>/molecule) given by the SRIM code (Ziegler *et al.*, 2008).

A Fourier-transform infrared (FTIR) spectrometer Vertex 70 by Bruker ( $10000\text{--}400 \text{ cm}^{-1} = 1\text{--}25 \mu\text{m}$ ) is interfaced to the UHV chamber through two KBr IR transparent windows. The spectrometer is placed on a moveable optical bench that allows a precise alignment of the IR beam with respect to the substrate. For this purpose, a hole is made on

the substrate holder that allows the IR beam of the spectrometer, transmitted by the ice film deposited on the substrate, to reach the detector. The substrate holder is inclined by  $45^\circ$  with respect to both the ion beam and IR beam directions; hence IR transmission spectra of the irradiated ices can be acquired *in situ* before, during, and after irradiation.

To prepare the organic samples for the PSS experiment, we used a C-, N-, and O-bearing ice mixture: N<sub>2</sub>:CH<sub>4</sub>:CO (1:1:1). In particular, we used Aldrich chemical CH<sub>4</sub>, CO, and Air Liquide N<sub>2</sub>. Three fill-pump down sequences were performed before introducing the mixture into the UHV chamber. This was done to prevent contamination of the mixture by the residual gas (mostly water vapor) present in the mixing chamber. Once deposited on a VUV transparent MgF<sub>2</sub> substrate (furnished by ESA) at 17 K, the ice mixtures were irradiated by 200 keV He<sup>+</sup> ions at a dose of 110 eV/16u. Under UHV condition, almost all the residual gas is made of molecular hydrogen that does not freeze on the substrate at 17 K. Hence, contamination, if any, could only come from the mixing chamber. Nevertheless, we were not able to recognize in the IR spectrum of the deposited ices any significant amount of possible contaminants such as H<sub>2</sub>O or CO<sub>2</sub>. We prepared a total number of 30 samples over three different thicknesses (10 samples for each thickness). The average values of the three thicknesses of the ice mixtures were  $1.322 \pm 0.02$ ,  $0.889 \pm 0.01$ , and  $0.456 \pm 0.01 \mu\text{m}$ , which correspond, under our experimental conditions, to interference curves of about 6, 4, and 2 fringes, respectively. The given uncertainties are the root mean squares on the corresponding 10 samples; their low values testify to the good reproducibility of the deposited ice mixtures' thickness. At the end of deposition, an FTIR spectrum of the ice mixture was acquired. Unless indicated otherwise, all the transmittance spectra reported in this article are given in optical depth scale. The optical depth ( $\tau$ ) was calculated by using the Beer-Lambert law:  $I = I_0 e^{-\tau}$  where  $I_0$  is the normalization continuum. An example of the IR spectra of the deposited ice mixtures for the three different thicknesses can be found

in the work of Baratta *et al.* (2015, see their Fig. 2). The presence of the CO (2140 cm<sup>-1</sup>) and CH<sub>4</sub> (3010 and 1300 cm<sup>-1</sup>) features is evident in the spectra. Molecular nitrogen is a homonuclear symmetric species; hence it has no IR active vibration. For this reason, no feature due to molecular nitrogen could be seen in the deposited ice film. The column density  $n$  (molecules/cm<sup>2</sup>) of the observed species can be calculated by using the relation

$$n = \left( \int_{\nu} \tau(\nu) d\nu \right) / A \quad (1)$$

where  $A$  represents the band strength (cm/molecule) and  $\int_{\nu} \tau(\nu) d\nu$  is the band area (cm<sup>-1</sup>) of a given band. The column density of CO and CH<sub>4</sub> for all the deposited ice mixtures was evaluated by Baratta *et al.* (2015). By supposing that the column density of N<sub>2</sub> was equal to the column density of both CO and CH<sub>4</sub> in the 1:1:1 (N<sub>2</sub>:CH<sub>4</sub>:CO) mixtures and by considering the measured thicknesses, Baratta *et al.* (2015) computed the density of the deposited ices. In particular, they found the following values: 0.68 g/cm<sup>3</sup> (6 fringes), 0.67 g/cm<sup>3</sup> (4 fringes), and 0.72 g/cm<sup>3</sup> (2 fringes). These values can be considered the same within the experimental uncertainties that are mainly due to the procedure used to compute the column density.

An irradiation dose of 110 eV/16u is representative of the dose that occurs in the external layers of comets and TNOs on timescales on the order of the age of the Solar System (Strazzulla *et al.*, 2003). This dose is within the dosage required for the conversion of low-molecular-weight hydrocarbons into refractory organic residues stable at room temperature (Strazzulla and Johnson, 1991). It is well known that ion irradiation induces several effects, including chemical changes (Hudson *et al.*, 2008; Palumbo *et al.*, 2008). The IR spectra of the ice mixtures after irradiation for the three considered thicknesses are reported in Fig. 2. The presence of many newly formed molecular species is evident. The strongest band of HCN ( $\nu_3$ , ~3130 cm<sup>-1</sup>) (Hudson and Moore, 2003) is superimposed over a multicomponent broad band observed between 3600 and 2600 cm<sup>-1</sup> (see bottom panel of Fig. 2). This broad feature is distinctive of many N–H, O–H, and C–H bands. The spectral region between 2400 and 2000 cm<sup>-1</sup> (top panel of Fig. 2) shows the presence of several new features, in particular ~2340 cm<sup>-1</sup> (CO<sub>2</sub>), ~2338 cm<sup>-1</sup> (N<sub>2</sub>), ~2260 cm<sup>-1</sup> (HNCO), ~2235 cm<sup>-1</sup> (N<sub>2</sub>O), ~2165 cm<sup>-1</sup> (OCN<sup>-</sup>), ~2101 cm<sup>-1</sup> ( $\nu_1$  HCN), ~2092 cm<sup>-1</sup> (CH<sub>2</sub>N<sub>2</sub>) (see, *e.g.*, Grim and Greenberg, 1987; Hudson *et al.*, 2001; Hudson and Moore, 2003; Palumbo *et al.*, 2004; Sicilia *et al.*, 2012). This attests to the complex chemistry induced by ion irradiation on simple molecular ices. For further details on the chemistry of the irradiated N<sub>2</sub>:CH<sub>4</sub>:CO ice mixture, the reader is referred to the work of Baratta *et al.* (2015).

Once irradiated, the frozen target was allowed to gently warm overnight and under vacuum to room temperature by switching off the cryostat. The day after, the organic residue was extracted from the chamber, and a blank MgF<sub>2</sub> window was mounted. We let the pumping system evacuate the chamber for at least 24 h before the MgF<sub>2</sub> window was cooled down to 17 K and another mixture was deposited and irradiated. This procedure was repeated for all the 30 samples prepared. After extraction from the chamber, an IR spectrum, from 8000 cm<sup>-1</sup> down to the cutoff limit of the

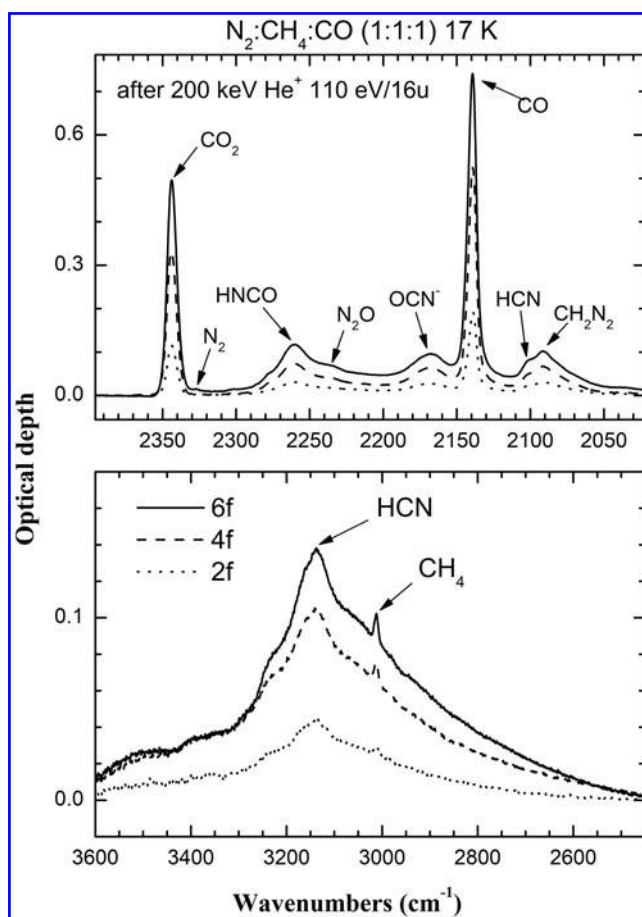
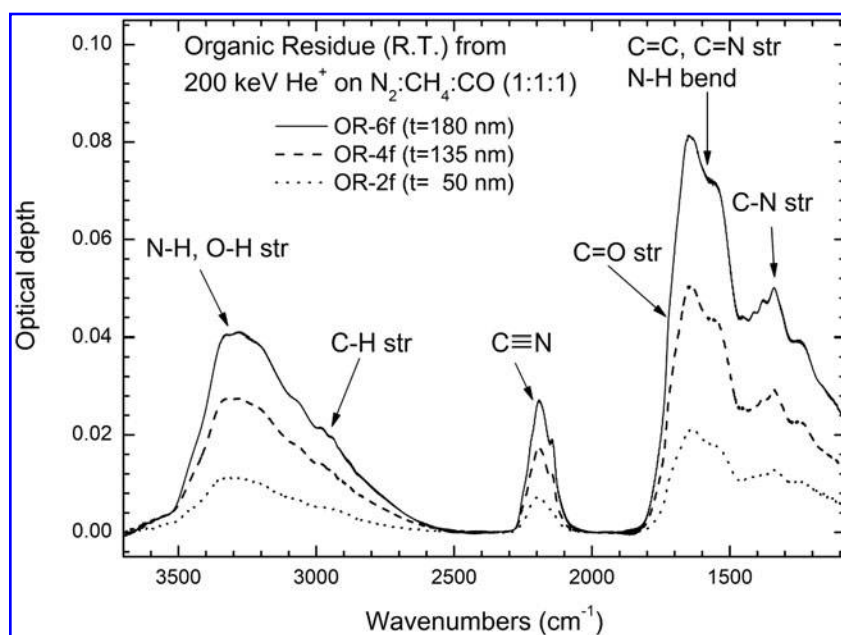


FIG. 2. Spectra after 200 keV He<sup>+</sup> irradiation of the ice mixtures for the three considered thicknesses.

MgF<sub>2</sub> window at 1000 cm<sup>-1</sup>, was obtained for each sample with a Bruker Equinox 55 FTIR spectrometer. No significant differences (standard deviation less than 2%) were observed between the IR spectrum acquired in air and the IR spectrum acquired in the chamber with the sample still under vacuum before extraction. In Fig. 3, the IR spectra of the organic residues obtained for the three considered thicknesses are reported. The labels 6f, 4f, and 2f in the figure indicate the organic residues obtained from irradiation of 6, 4, and 2 fringes “thick” ice mixtures, respectively. In the figure, the thicknesses of the organic residues are also indicated. It should be considered that the thicknesses of 0.050 μm (2f), 0.135 μm (4f), and 0.180 μm (6f) of the organic residues are average thicknesses over all the 30 PSS samples. To obtain a precise measurement of the thickness of each individual flight sample, we used the optical constants derived by Baratta *et al.* (2015) to generate theoretical spectra that have been compared with the spectra of the corresponding organic residues acquired just after their production. For each organic residue, the thickness was measured as that which provides the best match between the theoretical and the experimental spectra over an extended range (from the UV to the mid-IR). All the volatile species such as CO, CO<sub>2</sub>, N<sub>2</sub> sublimated during the slow warm-up to room temperature; hence the thicknesses of the residues are considerably reduced with respect to the thicknesses of the ice mixtures.



**FIG. 3.** Spectra of the organic residues obtained after irradiation at a dose of 110 eV/16u at 17 K followed by a slow warm-up to room temperature and sublimation of the volatile species. Each displayed spectrum is the average of the 10 different samples realized for each thickness.

Many features are present in the residues. We note that the IR spectra of the residues are quite similar to the IR spectra of many tholins prepared by radiofrequency (RF) plasma discharge of  $N_2:CH_4$  gas mixtures (Mutsukura and Akita, 1999; Imanaka *et al.*, 2004; Quirico *et al.*, 2008). The broad feature extending from 3500 to 2500  $cm^{-1}$  displays many subpeaks that can be assigned to N–H, O–H, and C–H stretching vibrations. This broad band is consistent with the presence of  $-NH_2$  and possibly  $-NH-$  functional groups of primary and secondary amine functions, respectively. In particular, features extending from 3500 to 3300  $cm^{-1}$  are consistent with  $NH_2$  groups connected to either aromatic or aliphatic functions, or both, while the peak at  $\sim 3220$   $cm^{-1}$  could be consistent with either  $ali-NH_2$  or a  $-NH-$  functional group (Quirico *et al.*, 2008). Subpeaks at  $\sim 2980$  and  $\sim 2940$   $cm^{-1}$  indicate the presence of  $-CH_3$  and  $-CH_2-$  stretching vibrations. The position of these peaks, shifted at higher wavenumbers with respect to that of alkyl chains, indicates the presence of  $CH_2$  and  $CH_3$  groups that are connected to nitrogen atoms, although the specific chemical groups involved cannot be identified (Quirico *et al.*, 2008).

The middle of the spectral range reveals a structured feature that peaks at  $\sim 2200$   $cm^{-1}$ . This feature is due to  $-C\equiv N$  (nitrile) and  $-N\equiv C$  (iso-nitrile) terminal groups (Mutsukura and Akita, 1999; Imanaka *et al.*, 2004); the carbodiimide function ( $-N=C=N-$ ) has also been proposed to give a contribution to this feature (Imanaka *et al.*, 2004). This structured feature also exhibits a well-resolved shoulder that peaks at  $\sim 2150$   $cm^{-1}$ . The shoulder is better resolved with respect to the other subpeaks observed, and its width is similar to that of the  $OCN^-$  feature detected in the irradiated ice mixture before warming up. Although the  $OCN^-$  feature peaks at 2165  $cm^{-1}$  at 17 K, its peak position shifts to lower wavenumbers, and its intensity significantly decreases during warm-up toward room temperature (Palumbo *et al.*, 2004; Accolla *et al.*, 2018). Hence, the shoulder seen at  $\sim 2150$   $cm^{-1}$  could be due to residual  $OCN^-$  trapped in the organic residue.

At lower wavenumbers, a structured broad asymmetric feature, peaking near 1600  $cm^{-1}$  and extending down to the cutoff limit of the  $MgF_2$  window, is present. In analogy to some tholins, the two main peaks at 1650–1630  $cm^{-1}$  and 1560  $cm^{-1}$  could be indicative of the presence of the following functional groups: C=C aromatics, C=N heteroaromatics, aromatic- and aliphatic- $NH_2$  bend (Imanaka *et al.*, 2004; Quirico *et al.*, 2008). A contribution to the 1630  $cm^{-1}$  feature could also be due to O–H bending vibrations. We noted the presence of a weak shoulder at 1710  $cm^{-1}$  that is due to C=O stretching vibrations. Three weak subpeaks are present at 1450, 1415, and 1380  $cm^{-1}$ ; the first two are probably due to the bending modes of the  $-CH_3$  and  $-CH_2-$  groups, which give rise to the stretching modes seen at  $\sim 2980$  and  $\sim 2940$   $cm^{-1}$ , while the peak at 1380  $cm^{-1}$  points to the presence of C– $CH_3$  or C– $(CH_3)_2$  groups (Quirico *et al.*, 2008). With regard to the remaining subpeaks, the feature that peaks at 1339  $cm^{-1}$  can be assigned to C–N (aromatic) stretching vibration (Imanaka *et al.*, 2004), while we were not able to identify the feature seen at 1240  $cm^{-1}$ . A summary of the IR features seen in the organic residue is reported in Table 1.

From this analysis, the chemical complexity exhibited by the organic residues becomes evident; in particular, many chemical groups have been assigned, although no specific molecular species have been recognized. Furthermore, we know that the residues probably contain complex species that have not been detected by IR spectroscopy. As an example, complex molecules such as succinonitrile ' $NCCH_2CH_2CN$ ', 3-aminocrotonitrile ' $(CH_3)C(NH_2)CHCN$ ', and so on have been identified in the organic residues obtained by ion irradiation of nitrile ( $CH_3CN$ ) containing ice; these astrobiologically relevant molecules have a very low abundance and have been identified by gas chromatography–mass spectroscopy, while they are difficult or even impossible to identify by IR spectroscopy (Hudson *et al.*, 2008). Furthermore, by comparing the results obtained on residues produced by UV photolysis and ion irradiation of different ice mixtures, Hudson *et al.* (2008) suggested that energetic processing of almost any ice

TABLE 1. ASSIGNMENT OF THE IR FEATURES OBSERVED IN THE ORGANIC RESIDUES

| Wavenumber (cm <sup>-1</sup> ) | Implied functional group                                 | Reference     |
|--------------------------------|--|---------------|
| 3500–3300                      | ali-NH <sub>2</sub> , aro-NH <sub>2</sub> str.           | (a)           |
| 3220                           | ali-NH <sub>2</sub> , -NH- str.                          | (a)           |
| 2980                           | -CH <sub>3</sub> str.                                    | (a)           |
| 2940                           | -CH <sub>2</sub> - str.                                  | (a)           |
| 2200                           | -C≡N, -N≡C,<br>-N=C=N-                                   | (b, c)<br>(c) |
| 2150                           | OCN <sup>-</sup>   | (d)           |
| 1710                           | C=O str.   | (a)           |
| 1650–1630, 1560                | arom. C=C, he-arom. N=C<br>ali-/aro-NH <sub>2</sub> bend | (a, c)        |
| 1450                           | -CH <sub>3</sub> bend                                    | (a)           |
| 1415                           | -CH <sub>2</sub> - bend                                  | (a)           |
| 1380                           | C-CH <sub>3</sub> , C-(CH <sub>3</sub> ) <sub>2</sub>    | (a)           |
| 1339                           | C-N arom. str.   | (c)           |
| 1240                           | unidentified   |               |

References: (a)=Quirico *et al.*, 2008; (b)=Mutsukura and Akita, 1999; (c)=Imanaka *et al.*, 2004; (d)=Palumbo *et al.*, 2004.

mixture containing C, H, N, and O atoms probably results in the formation of amino acid precursors that, if hydrolyzed, give rise to the amino acids themselves. Similar conclusions have been drawn by Materese *et al.* (2014), who found, in the organic residue of a far-UV irradiated N<sub>2</sub>:CH<sub>4</sub>:CO (100:1:1) ice mixture, complex molecules such as glyceric acid, lactic acid, urea, and so on. Hence, even if IR spectroscopy does not reveal them due to its relatively low sensitivity (Hudson *et al.*, 2008; Materese *et al.*, 2014), complex molecules of astrobiological interest are probably present in the organic residues described in this work.

In addition to FTIR spectroscopy, the 30 organic samples were characterized by VUV and UV-vis-NIR transmission spectroscopy. In particular, on the basis of the transmission spectra acquired on the 30 samples over the three different thicknesses, Baratta *et al.*, (2015) derived the optical constants (*n* and *k*) of the organic residue in the range of 500–84,000 cm<sup>-1</sup> by adopting the Kramers-Kronig constrained variational dielectric function (KKCVDF) fitting procedure (Kuzmenko, 2005). In particular, Baratta *et al.* (2015) obtained a Kramers-Kronig constrained set of optical constants as the best fit solution to the experimental transmission spectra together with the three average best fit thicknesses of the 6f, 4f, and 2f residues. The optical constants of the organic residue are available online at the link <http://www.oact.inaf.it/weboac/labsp/ORPSS.html>.

## 2.2. Exposure on the ISS

The samples of all the experiments of the EXPOSE-R2 mission were placed in special carriers accommodated in three different trays; in particular, all the PSS samples were placed in tray number 3 (Rabbow *et al.*, 2017). PSS samples, placed in individual sample containers called cells, were integrated in two stacked carrier layers each in three compartments of tray 3. Only the samples in the top carriers were exposed to the solar UV radiation, while the

samples in the underlying carriers were completely shaded, providing the respective “in-flight” dark controls. Three temperature sensors were attached to the bottom side of each tray. In addition, tray 3 was equipped with the active dosimetry R3D-R2, a radiation sensor package for ionizing radiation and UV measurements. Environmental data of the EXPOSE-R2 mission (temperatures, UV exposure, etc.) were collected every 10 s and stored and downlinked as telemetry.

On the night of 23 July 2014, the cargo 56P progress carrying the three trays of the EXPOSE-R2 mission was launched from Baikonur (Kazakhstan) to the ISS. After docking on 24 July 2014, the three trays were stored inside the ISS. On 6 August, the trays were integrated in the monoblock EXPOSE-R2 that remained inside the ISS until it was installed outside on the URM-D platform, during the extravehicular activity (EVA)-39 on 18 August 2014. The vacuum exposure period of the mission began on 20 August 2014, when the venting valves of the still covered EXPOSE-R2 were opened remotely by the Mission Control Center in Moscow. During the next 62 days, EXPOSE-R2 was subjected to an outgassing period while shielded from solar UV irradiation. On 22 October 2014, the EXPOSE-R2 cover was removed during EVA-40, starting the UV exposure of the experiments. Solar UV exposure ended on 3 February 2016, when EXPOSE-R2 was returned to the ISS interior during EVA-42. On 2 March 2016, tray 3 landed at Karaganda (Kazakhstan), on board the Soyuz 44S return capsule. The exposure of the samples to solar UV radiation in low Earth orbit outside the ISS lasted 469 days, while the total exposure to space vacuum was 531 days.

In parallel to the space experiment, a Mission Ground Reference (MGR) experiment was performed at the German Aerospace Center (DLR), Cologne, Germany. The experiment used a set of trays and carriers similar to those exposed outside the ISS. In particular, three ground trays identical to the flight trays, with respect to the sample interface, were loaded with a full set of samples identical to the flight ones. The trays were placed in a temperature-controlled interface and connected to the vacuum facility of the PSI (Planetary and Space Simulation Facilities) at DLR. Automated temperature simulation of the MGR trays started with application of transport temperatures. As soon as the EXPOSE-R2 temperatures in orbit became available by telemetry, they were applied and updated every 10 s, with a maximum delay of 2 months due to the reformatting and analysis process of data. The highest and lowest temperatures experienced by EXPOSE-R2 trays in orbit were 58°C (tray 3, compartment 4) and -20.9°C (tray 3, compartment 2), respectively. In orbit, temperature fluctuations follow warm periods (temperatures up to 50°C on average), which are followed by cold periods (temperatures down to -20°C on average) with a slow periodicity of about 1 month due to the variation of the ISS orbital plane. Superimposed to this slow variation, EXPOSE-R2 trays experienced a fast variation of temperature, with a periodicity of nearly 90 min due to the ISS day/night times of each orbit. Day/night temperature fluctuations were approximately 10°C during warm periods and a few degrees during cold periods.

As in space, only the top carriers of the EXPOSE-R2 MGR were irradiated with a SOL2000 metal halide lamp-based solar simulator (by Dr. Hönle GmbH), which provided

a continuum spectrum with wavelength  $>200$  nm; the spectral irradiance of the solar simulator can be found in Fig. 3 in the work of Onofri *et al.* (2008). The MGR tray compartments were irradiated at ground individually with the same UV fluences accumulated by the EXPOSE-R2 trays outside the ISS during the entire mission. Unfortunately, due to a malfunction of the system, irradiation was not performed under vacuum. The UV fluences were provided by RedShift Design and Engineering BVBA, Belgium, contracted by ESA (calculated UV radiation fluence data). It should be noted that the samples were not always facing the Sun because the ISS orbits around Earth and changes its orientations relative to the Sun. In addition, shadows by solar panels and the ISS environments in the vicinity of the EXPOSE-R2 facility (radiators, etc.) significantly decrease the effective insulation. The orientation of the ISS has been computed and the UV fluence at each sample position has been evaluated taking into account the daily variation of insulation along the whole mission duration. The UV sensor data have been used to verify the adopted models. The variation of the solar irradiance due to the eccentricity of the Earth orbit and to the solar activity has also been taken into account. This was done by RedShift considering the actual solar spectrum, averaged along the mission duration, measured by the satellite SORCE. The transmittance of the windows, weighted by the solar spectrum, has also been considered. Hence the mean UV fluence for samples in each compartment has been determined. Fluences, in the wavelength range (200–400 nm), have been applied individually on the corresponding compartment and experiment during the MGR. In order to find out any possible modification induced by the thermal cycles experienced in orbit and at ground, in the case of the PSS experiment, an additional ground reference full set of samples has been stored under vacuum at a constant temperature of 5°C during the MGR for comparison. The scheme showing the experimental breakdown of samples between the ISS and DLR Cologne and the environmental conditions to which they have been exposed is reported in Fig. 1b.

With regard to our samples, as previously indicated, we prepared 30 organic residues that had three different thicknesses (10 samples for each thickness). Twelve of them were accommodated in EXPOSE-R2 outside the ISS. In particular, two samples for each thickness (six in total) were exposed in the top carrier of tray 3 to solar UV photons, ionizing cosmic radiation, and temperature cycling. The remaining flight samples (two for each thickness) were placed in the underlying carrier where they were exposed only to ionizing cosmic radiation and temperature cycling, providing the in-flight dark controls. The remaining 18 samples were part of the ground MGR simulation experiment. Referring to the ground samples, two samples for each thickness were exposed to the PSI solar simulator and temperature cycling in the top carrier of EXPOSE-R2 MGR facilities, whereas the other two dark control samples for each thickness were exposed only to temperature cycling in the underlying carrier. Lastly, the remaining two ground samples for each thickness were stored under vacuum at 5°C.

Following the work of Baratta *et al.* (2015), we evaluate here the irradiation doses suffered by the flight exposed organic residues. Ultraviolet photons (*i.e.*,  $E > 3.1$  eV,  $\lambda <$

400 nm) have enough energy to break chemical bonds and initiate substantial chemical changes (Stern, 2003), where a photon energy of 3 eV corresponds to the dissociation threshold in the gas phase of relatively weak bounded species such as  $\text{CH}_2$  (Heays *et al.*, 2017).

By considering the absorption coefficient of the organic residue (Baratta *et al.*, 2015) and the ASTM E-490 standard solar spectrum for space application (that is given down to  $\lambda = 119.5$  nm) over the range ( $119.5 < \lambda < 400$  nm), the UV irradiation dose suffered by the 2f (50 nm) organic residue over the 2111 h of equivalent to perpendicular solar irradiation, as determined by RedShift, is  $4.7 \times 10^5 \pm 5\%$  eV/16u. If we consider only the more energetic, VUV, solar photons ( $E > 6.2$  eV,  $\lambda < 200$  nm), the irradiation dose over the range ( $119.5 < \lambda < 200$  nm) is  $1.2 \times 10^3 \pm 14\%$  eV/16u. The errors given derive from the uncertainties associated with the equivalent to perpendicular solar irradiation exposure time; they were provided by RedShift and depend on the particular frequency band considered. The main sources of uncertainties are as follows: the geometrical model (depends on sample position), window transmission (depends on the frequency band), variation in solar irradiance (depends on the frequency band), and reflections (depend on sample position and the frequency band). For the EXPOSE-R2 mission, the total contribution of ionizing radiation given by GCRs, South Atlantic Anomaly protons, and outer radiation belt electrons reached dose values up to 1 gray (Gy) (Rabbow *et al.*, 2017). One gray corresponds to  $1.7 \times 10^{-7}$  eV/16u; hence the effects given by ionizing radiation are negligible with respect to those given by solar UV photons, even by considering only the more energetic ( $E > 6.2$  eV) solar photons.

An accurate description of the EXPOSE-R2 and MGR hardware and of the different mission phases can be found in the work of Rabbow *et al.* (2017).

### 3. Results

#### 3.1. Comparison between the sample controls

The postflight FTIR, UV-vis-NIR, and VUV spectra of the organic residues were acquired by using the same conditions (*i.e.*, resolution, sampling, etc.) that were adopted for the preflight samples. In this article, we focus on the results obtained by FTIR spectroscopy. In particular, FTIR spectra were acquired in air at normal incidence, with a resolution of  $1 \text{ cm}^{-1}$  and a sampling of  $0.25 \text{ cm}^{-1}$ . Every sample on the ISS and at ground was realized in duplicate. We observed no significant differences in the profile of the IR features between the duplicates, and only a small variation in the intensity of the IR features was observed. In particular, with regard to all the duplicates, we found an average percentage variation of the intensities of the 3220, 2200, and  $1600 \text{ cm}^{-1}$  features of  $10\% \pm 6\%$ ,  $10\% \pm 8\%$ , and  $12\% \pm 9\%$ , respectively. To improve the signal-to-noise ratio of the IR spectra of the organic residues, in the following for any thickness and typology, we use the average spectrum obtained from the duplicates.

In Fig. 4, a comparison between the in-flight dark controls and the DLR (MGR) controls is reported for the three different thicknesses. From Fig. 4 it is evident that, for each thickness, no systematic differences can be found between the controls. In particular, the differences observed between

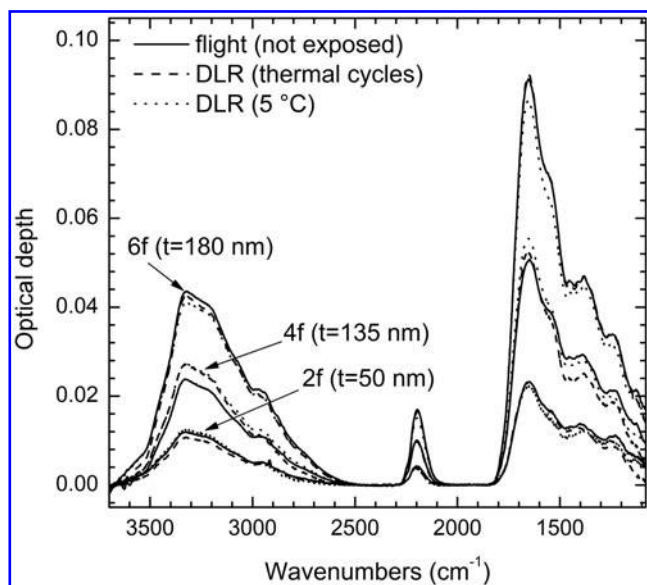


**FIG. 4.** Comparison between the spectra of the ground and in-flight dark controls.

the IR spectra of different controls are similar to the differences found between the IR spectra of duplicates. Hence, the organic residues are very stable with respect to the temperature cycles experienced in orbit. On the other hand, by comparing Fig. 4 and Fig. 3, a decreased intensity of the  $\text{C}\equiv\text{N}$  feature at  $\sim 2200\text{ cm}^{-1}$  with respect to the other two main broad features at  $\sim 3220$  and  $\sim 1600\text{ cm}^{-1}$  and the disappearance of the  $\sim 2150\text{ cm}^{-1}$  shoulder is evident in the postflight samples. To discern any temporal modification of the FTIR spectra of the organic residues that we prepared for the PSS experiment, we also prepared an additional set of samples identical to the flight ones that we monitored by FTIR spectroscopy during the EXPOSE-R2 mission. We found that the two main broad features displayed very small changes, while the  $\text{C}\equiv\text{N}$  feature decreased at a rate that was fast at the beginning but slower and slower with time. We verified that the fast decrease of the  $\text{C}\equiv\text{N}$  feature, observed for several days after the production of the residue, occurred as well for the organic residues kept under UHV condition. In Fig. 5, the band area of the  $\text{C}\equiv\text{N}$  feature of the lab-control organic residues is reported versus the time elapsed since their production. In the same figure, the band area obtained for the flight control PSS residues is also reported. Note that in order to minimize any possible damage or contamination, only the band area obtained just after the production of the organic residue was measured for the flight samples. Indeed, just after their production and spectra acquisition, all the PSS organic residues were stored in special Teflon containers thought to preserve the samples from moisture, contamination, and damage. All our samples are, at present, still stored in these containers. After the end of the mission, two additional spectra were acquired. For each thickness, the lab-control and flight-control samples showed a common trend in Fig. 5. In particular, after a fast decrease at the beginning, the  $\text{C}\equiv\text{N}$  feature band area almost stabilizes after 200 days and did not vary further, within uncertainties, after 700 days. The two vertical dashed lines in

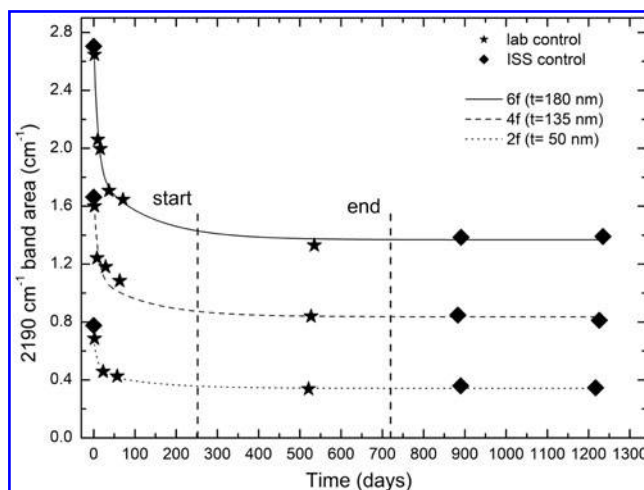


**FIG. 5.** Temporal evolution of the  $2200\text{ cm}^{-1}$  ( $\text{C}\equiv\text{N}$ ) band area of the laboratory and in-flight control unexposed samples. The two dashed vertical lines correspond to the start and the end of exposure to the solar UV photons experienced in orbit by the exposed samples. The best fit to the data was obtained by using the equation  $y = sc*(y_0 + A1*\exp(-t/t1) + A2*\exp(-t/t2))$ . Once the best fit solution was found for the thickest (6f) samples with  $sc$  set to 1, the other two thicknesses were fitted by adjusting only the  $sc$  scaling factor.

the figure indicate the start and the end of exposure outside the ISS; hence the organic residues were already stabilized during exposure to the solar UV photons. The reason for the decrease of the  $2200\text{ cm}^{-1}$  feature is not clear. It could be either due to some volatile, that is,  $\text{C}\equiv\text{N}$  bearing species that leave the residue, or to the reaction and modification of a  $\text{C}\equiv\text{N}$  bearing species with other species in the matrix. If the shoulder seen at  $\sim 2150\text{ cm}^{-1}$  in the preflight organic residues is actually due to  $\text{OCN}^-$ , the reduction of the intensity of the  $2200\text{ cm}^{-1}$  feature could have an alternative explanation. In particular, we know that ion irradiation of a different mixture ( $\text{N}_2:\text{CH}_4:\text{H}_2\text{O}$ , 1:1:1) leads to the formation of an organic residue that exhibits a feature peaking at  $2158\text{ cm}^{-1}$ , with a different profile with respect to the  $2200\text{ cm}^{-1}$  feature seen in the PSS organic residues that is attributed to  $\text{OCN}^-$  (Accolla *et al.*, 2018). The authors observed that, in those experiments, the  $\text{OCN}^-$  feature exhibits a gradual reduction in intensity over time, decreasing by 60% after 2 weeks and almost by 100% after 150 days, that is, with a similar timescale of the reduction of the  $2200\text{ cm}^{-1}$  feature. Hence, it is possible that the decrease of the  $2200\text{ cm}^{-1}$  feature seen in the PSS organic residues is due to the decrease of the  $\text{OCN}^-$  ion/salt either desorbing or reacting with time. After the complete disappearance of the  $\text{OCN}^-$  from the matrix, the  $2200\text{ cm}^{-1}$  does not change further, which indicates that the nitriles/isonitriles terminal groups are stable in the organic residue.

### 3.2. Space-exposed organic residues

In Fig. 6, a comparison between the IR spectra of the flight solar UV-exposed organic residues (solid lines) and the corresponding in-flight dark controls (dotted lines) is reported for the three considered thicknesses. The presence

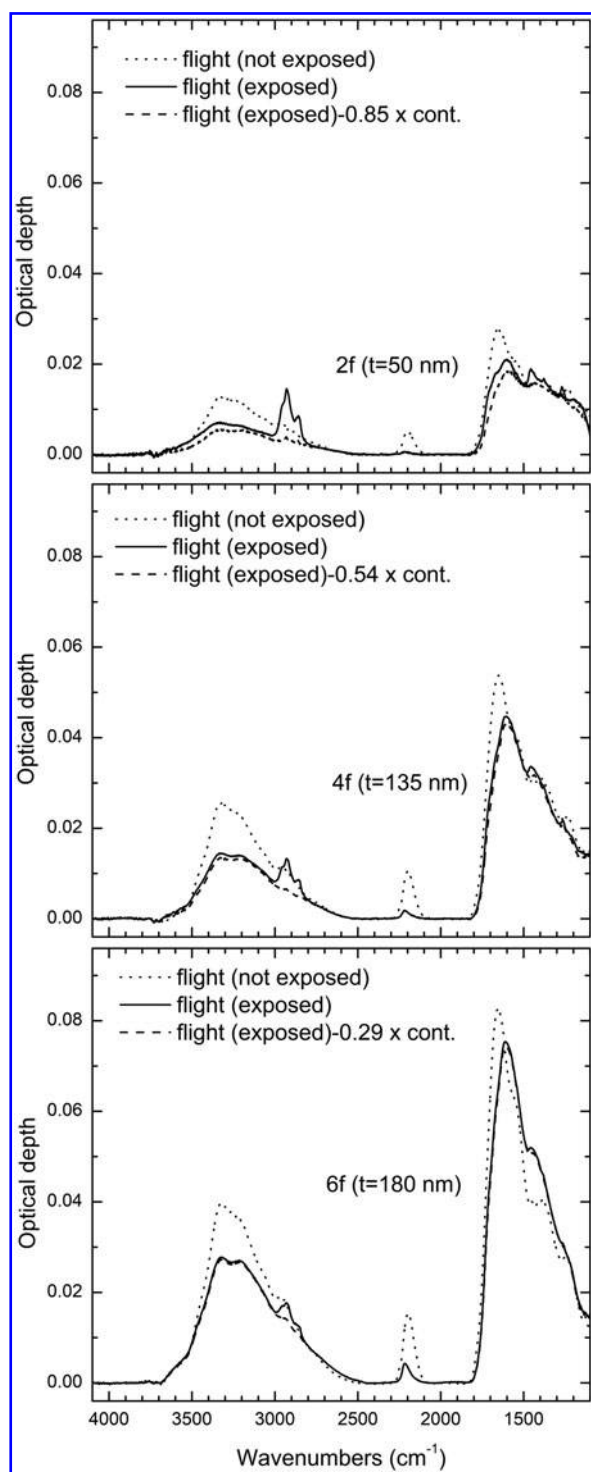


**FIG. 6.** Comparison between the in-flight dark controls (dotted lines) and the flight exposed samples before (solid lines) and after (dashed lines) the correction for the contamination spectrum.

of relatively strong  $-\text{CH}_3$  and  $-\text{CH}_2-$  stretching features ( $2950$ ,  $2930$ , and  $2860\text{ cm}^{-1}$ ) and bending features ( $1458$  and  $1380\text{ cm}^{-1}$ ) is evident in the exposed samples. We notice that the intensity of these features is inversely correlated with the thickness of the samples, and the features are not observed in the in-flight dark controls. As was already

observed for the former EXPOSE-R mission (Demets *et al.*, 2015), the aliphatic features are due to a contamination layer deposited on the inner side of the solar exposed  $\text{MgF}_2$  windows. It is thought that the contamination is due to the release of outgassing products from the facility itself and its samples, which were subsequently photoprocessed by solar UV at the inner window surfaces into a thin contamination layer (Rabbow *et al.*, 2017). In general, the contamination observed on EXPOSE-R2 seems to be lesser than after the EXPOSE-R mission. This improvement was due substantially to three reasons: (1) EXPOSE-R2 used the EXPOSE-R module that has been already outgassing in orbit during the EXPOSE-R mission, (2) the duration of exposure to solar UV was shorter for EXPOSE-R2, (3) EXPOSE-R2 has been subjected to a 62-day outgassing period while shielded from solar UV irradiation; this procedure has not been previously adopted for EXPOSE-R (Rabbow *et al.*, 2017). It should be noted that the organic residues are on the internal surfaces of the  $\text{MgF}_2$  windows; thus the contamination layer is accreted on the organic residues from the opposite side with respect to that exposed to solar UV photons. Hence, the contamination layer did not interfere with the solar UV exposure. To “clean” the spectra from the contaminant features, we acquired a transmission spectrum of a flight exposed  $\text{MgF}_2$  clean (blank) window on which the contamination layer was formed. Once normalized to the continuum and converted in optical depth units, the contamination spectrum was subtracted from each sample thickness by using a different scaling factor that was chosen to minimize the contribution of the contaminant CH features on the residual spectra. The corrected flight exposed sample spectra are reported in Fig. 6 with dashed lines. We notice that the contaminant features almost disappear in the corrected spectra. Furthermore, thicker residues correspond to thinner contamination layers. On the other hand, thicker organic residues absorb more UV light; hence the contamination layers can be considered to have a common composition and different thicknesses that are directly related to the UV fluences transmitted by the  $\text{MgF}_2$  plus organic residues assemblies.

From the comparison between the flight exposed and the in-flight dark control samples we notice the following: (1) An overall decrease in the exposed samples of the two main broad features and of the  $-\text{C}\equiv\text{N}$  feature for all the thicknesses except for the thickest 6f sample. In particular, an increase in intensity of the broad  $1600\text{ cm}^{-1}$  feature was observed in the region between  $1600$  and  $1240\text{ cm}^{-1}$ , for the 6f sample. (2) The thinner the sample, the stronger the reduction of intensity for the two main broad features and for the  $-\text{C}\equiv\text{N}$  feature. (3) The reduction in intensity of the features is accompanied by more or less evident changes of the profile of the bands. All these effects are particularly evident in the  $2200\text{ cm}^{-1}$   $-\text{C}\equiv\text{N}$  feature.

It should be noted that the solar UV flux is exponentially attenuated into the film; hence thinner residues received higher average UV doses. The higher UV doses absorbed by thinner residues explains why the relative reduction of intensity of the features increases from the thickest 6f to the thinnest 2f organic residue. In Fig. 7, the normalized spectra of the in-flight dark controls and the flight exposed samples are presented. Very small differences, having standard deviation with respect to the average normalized spectrum of

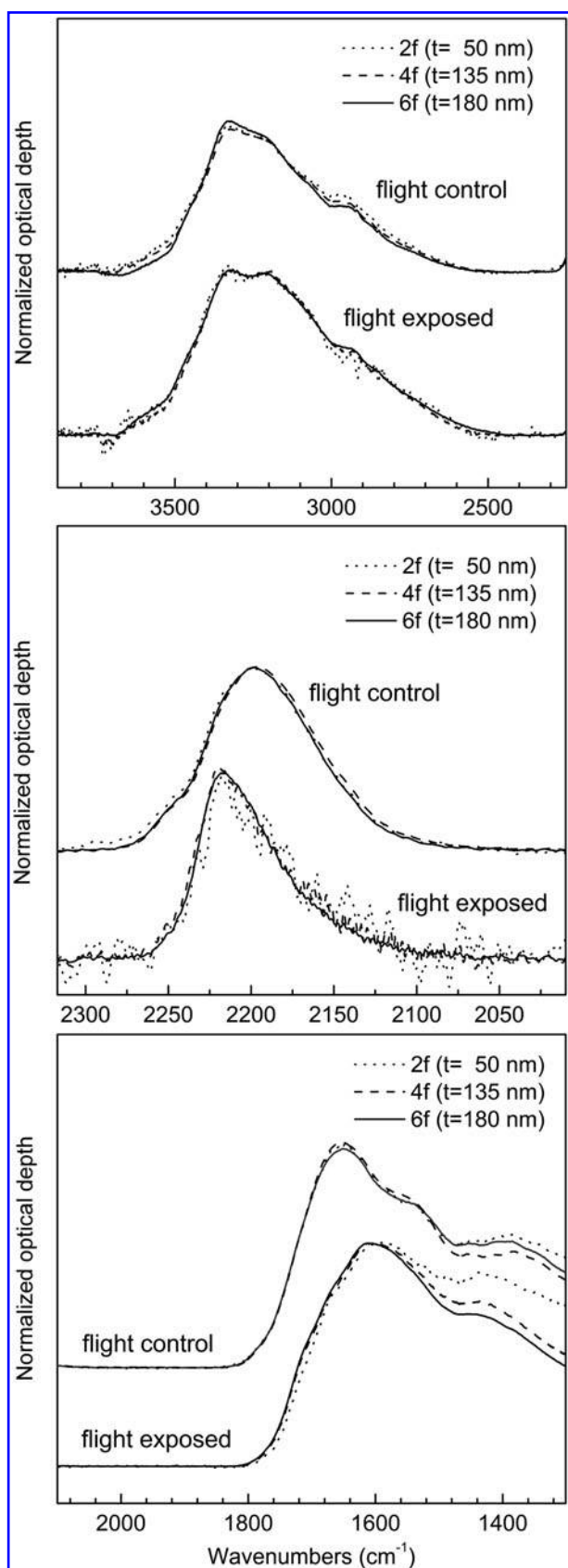


**FIG. 7.** Comparison of the normalized spectra, for the three different thicknesses, between the in-flight dark controls (upper curves) and the flight exposed (lower curves) samples in the three spectral regions of interest.

about 2%, are evident in the profile of the main features for the three considered thicknesses in the flight control samples; this points out that the organic residue is quite homogeneous versus the thickness as already observed by Baratta *et al.* (2015). On the other hand, a variation of profile of the 3220, 2200, and 1600 cm<sup>-1</sup> features is evident in the exposed samples with respect to the dark controls. Nevertheless, for the 3220 and 2200 cm<sup>-1</sup> features, the profile is very similar for the three different thicknesses in the flight exposed samples. Hence, the relative abundance of the species that contribute to the 3220 cm<sup>-1</sup> ( $-\text{NH}_2$ ,  $-\text{NH}-$ , etc.) and 2200 cm<sup>-1</sup> ( $-\text{C}\equiv\text{N}$ ,  $-\text{N}\equiv\text{C}$ , etc.) features changes at low UV irradiation doses but does not change further at higher doses from the thickest 6f to the thinnest 2f flight exposed organic residue. On the other hand, the profile of the 1600 cm<sup>-1</sup> ( $\text{C}=\text{C}$ ,  $\text{C}=\text{N}$ , etc.) feature still changes up to the highest doses corresponding to the 2f thinnest sample. A possible explanation for this trend is given in the discussion section.

### 3.3. VUV, UV-vis-NIR spectroscopy

The transmission spectra of the flight exposed samples in the UV-vis-NIR and VUV range were also acquired. Although the contaminant layer deposited on the inner side of the flight exposed samples did not interfere with the solar UV exposure, it strongly affects the transmission spectra in the UV-vis range. This was evident when we acquired the transmission spectra of the contaminated flight exposed blank MgF<sub>2</sub> window (see Section 3.2) in the UV-vis-NIR and IR range. To clean the UV-vis-NIR spectra, we followed the same procedure described in Section 3.2 using the same scaling factors determined for the IR spectra. We found that, in the vis-NIR range between 400 and 1200 nm, the absorption coefficient increases with the dose from the thickest (6f) to the thinnest (2f) sample. Only small differences of the absorption coefficient (within 7%) were found, between the different thicknesses, in the UV range (200–400 nm). Nevertheless, unlike the IR case, we could not perform any normalization to the continuum to correct the spectra. This is because the variations of transmittance due to the variation of absorption and continuum (dispersion and interference effects) cannot be easily disentangled in the UV-vis range. Hence, the conclusions given above on the variation of the absorption coefficient must be considered indicative.

### 3.4. The 2200 cm<sup>-1</sup> feature

Since the 2200 cm<sup>-1</sup> feature does not overlap with any other feature, we can try to obtain semiquantitative information on the relative abundances of  $-\text{C}\equiv\text{N}$  and  $-\text{N}\equiv\text{C}$  species by adopting a fit procedure (Quirico *et al.*, 2008). We were able to obtain a good fit by using five Gaussian components with peak positions similar to those used by Mutsukura and Akita (1999). In Fig. 8, the best fit to the 2200 cm<sup>-1</sup> feature for the 6f flight control and flight exposed samples is reported. The best fit output parameters and the corresponding uncertainties are reported in Table 2. Following the work of Mutsukura and Akita (1999), the peaks at 2105, 2145, and 2190 cm<sup>-1</sup> are associated to terminal  $-\text{N}\equiv\text{C}$  iso-nitrile units, while the peaks at 2220 and 2252 cm<sup>-1</sup> are associated to terminal  $-\text{C}\equiv\text{N}$  nitrile units.

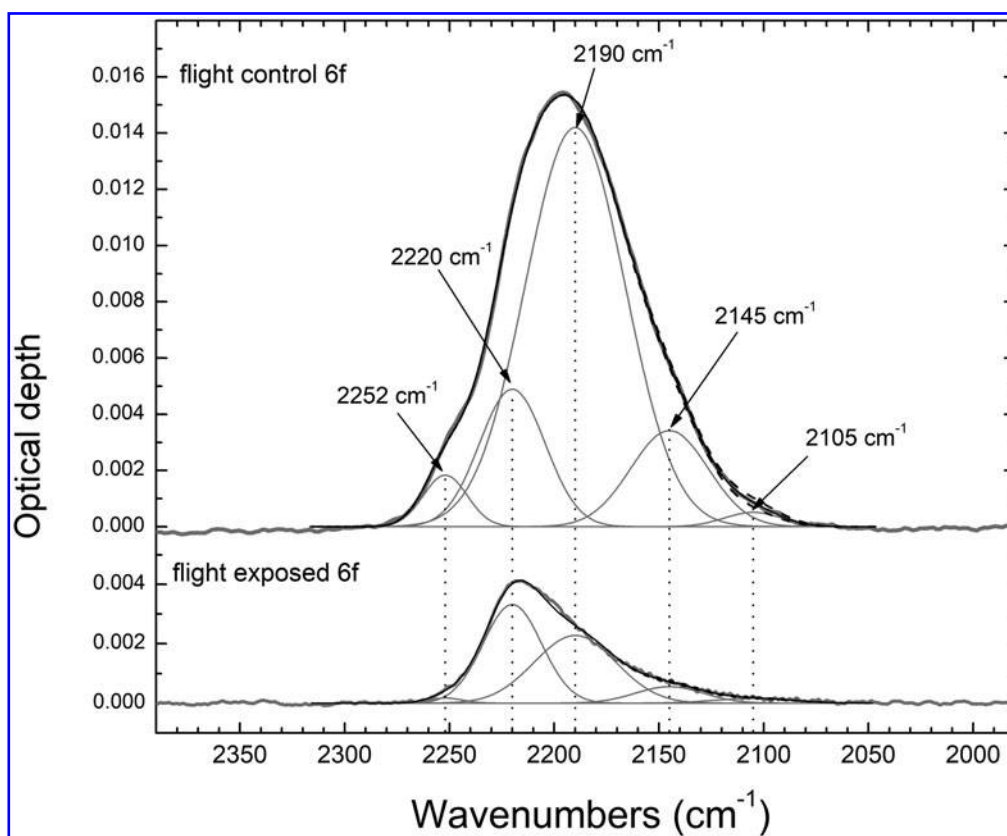


**FIG. 8.** Five Gaussians with fixed peak position (thin gray lines) best fit (thick gray lines) of the thickest 6f in-flight dark control (upper curves) and flight exposed (lower curves) samples. The 95% confidence interval of the best fit is indicated with black dashed lines. The best fit output parameters and their uncertainties are reported in Table 2.

By assuming that the band strength of the five subcomponents is the same, we obtain a relative amount of nitrile over iso-nitrile terminal units ( $-\text{C}\equiv\text{N}/-\text{N}\equiv\text{C}$ ) of 0.23 and 0.9 before and after UV space exposure, respectively. Nevertheless, these relative amounts should be considered as indicative for two reasons: (1) according to Quirico *et al.* (2008), conjugation can lower the nitrile band position down to  $2180\text{ cm}^{-1}$ , in this case the  $2190\text{ cm}^{-1}$  subcomponent would be due to a nitrile terminal unit; (2) the band strength can be different for the five subcomponents.

By using the spectra obtained for the three different thicknesses, it is possible to discern the effect of solar UV photons at different depths in the organic residue. In par-

ticular, following the work of Baratta *et al.* (2002), we indicate with  $\tau_{2f}$ ,  $\tau_{4f}$ , and  $\tau_{6f}$  the optical depths of the 2f, 4f, and 6f organic residues, respectively. Since the residues have been exposed to the same UV fluences, the optical depth of the slab at a depth between 50 nm (2f) and 135 nm (4f) is given by the relation  $\tau_{4f-2f} = \tau_{4f} - \tau_{2f}$ , and the optical depth of the slab between 135 and 180 nm (6f) is given by:  $\tau_{6f-4f} = \tau_{6f} - \tau_{4f}$ . In Fig. 9, the spectra of the slabs at different depths for the flight exposed and in-flight dark control organic residues are reported. From Fig. 9, it is evident that the decrease in intensity of the  $2200\text{ cm}^{-1}$  feature is larger at lower depths into the organic residue; hence deeper layers received a lower UV dose.

**TABLE 2.** FIVE GAUSSIAN CURVES BEST FIT PARAMETERS OF THE  $2200\text{ cm}^{-1}$  FEATURE OBSERVED IN THE 6F FLIGHT CONTROL AND 6F FLIGHT EXPOSED ORGANIC RESIDUES

| Peak position ( $\text{cm}^{-1}$ ) | Assignment                | Flight control area ( $\text{cm}^{-1}$ ) | Flight control FWHM ( $\text{cm}^{-1}$ ) | Flight exposed area ( $\text{cm}^{-1}$ ) | Flight exposed FWHM ( $\text{cm}^{-1}$ ) |
|------------------------------------|---------------------------|--|--|--|--|
| 2105                               | $-\text{N}\equiv\text{C}$ | $0.0179 \pm 0.0006$                      | $32.6 \pm 0.6$                           | $0.0075 \pm 0.0002$                      | $44.5 \pm 1$                             |
| 2145                               | $-\text{N}\equiv\text{C}$ | $0.159 \pm 0.003$                        | $43.7 \pm 0.6$                           | $0.0228 \pm 0.0006$                      | $38.5 \pm 0.9$                           |
| 2190                               | $-\text{N}\equiv\text{C}$ | $0.847 \pm 0.006$                        | $56.1 \pm 0.4$                           | $0.111 \pm 0.001$                        | $46.0 \pm 0.6$                           |
| 2220                               | $-\text{C}\equiv\text{N}$ | $0.193 \pm 0.004$                        | $36.9 \pm 0.6$                           | $0.1165 \pm 0.001$                       | $32.9 \pm 0.3$                           |
| 2252                               | $-\text{C}\equiv\text{N}$ | $0.0483 \pm 0.001$                       | $24.7 \pm 0.3$                           | $0.0037 \pm 0.0003$                      | $19.9 \pm 0.6$                           |

For each Gaussian curve, the full width at half maximum (FWHM) and the band area are reported. The peak positions of the curves (fixed) and the corresponding assignment (Mutsukura and Akita, 1999) are also reported in the table.

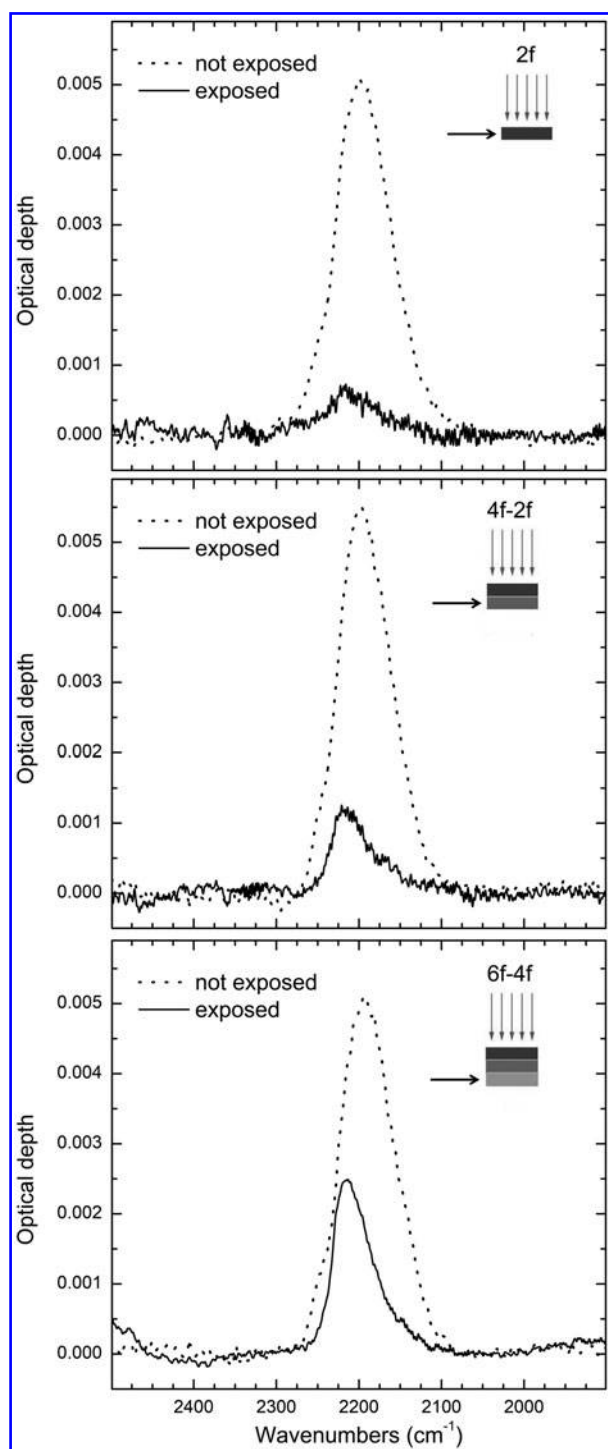


**FIG. 9.** Comparison of the  $2200\text{ cm}^{-1}$  CN feature between the in-flight dark control (dotted lines) and flight exposed (solid lines) samples at different depths (see the text).

To evaluate the lifetime at 1 AU of the  $-\text{C}\equiv\text{N}$  plus  $-\text{N}\equiv\text{C}$  bearing species versus the depth in the organic residue, we assume that the cumulative band area is proportional to the number of  $-\text{C}\equiv\text{N}$  plus  $-\text{N}\equiv\text{C}$  terminal units and the band strength is  $4.0 \times 10^{-17}\text{ cm/molecule}$  (Demyk *et al.*, 1998). In the following, we also use the suffix CN to mean the cumulative number of  $-\text{C}\equiv\text{N}$  and  $-\text{N}\equiv\text{C}$  terminal units.

We assume that the decrease of the number of CN can be described by an exponential decay, in particular

$$dN_{\text{CN}} = N_{\text{CN}}^0 e^{-\phi_{\text{UV}}^{\text{eff}}(x)t\sigma(\text{CN})} dx \quad (2)$$

where  $dN_{\text{CN}}$  is the number of CN per square centimeter contained in a layer of thickness  $dx$  after an exposure time  $t$  at a depth  $x$  in the organic residue;  $\phi_{\text{UV}}^{\text{eff}}(x)$  is the effective UV flux at a depth  $x$ ;  $\sigma(\text{CN})$  is the destruction cross section and  $N_{\text{CN}}^0$  is the number density of CN ( $\text{cm}^{-3}$ ) before exposure. We can also write

$$\phi_{\text{UV}}^{\text{eff}}(x) = \phi_{\text{UV}}^{\text{eff}}(0) e^{-\alpha(\text{UV})_{\text{eff}}x} \quad (3)$$

where  $\phi_{\text{UV}}^{\text{eff}}(0)$  is the incoming effective UV flux and  $\alpha(\text{UV})_{\text{eff}}$  is the effective UV absorption coefficient. If we indicate the decay rate with  $\Gamma = \phi_{\text{UV}}^{\text{eff}}(0) \cdot \sigma(\text{CN})$ , by integrating (Eq. 2), we obtain

$$n_{\text{CN}} = \int_{x_1}^{x_2} dN_{\text{CN}} = N_{\text{CN}}^0 \int_{x_1}^{x_2} e^{-\Gamma t} e^{-\alpha(\text{UV})_{\text{eff}}x} dx \quad (4)$$

where  $n_{\text{CN}}$  is the column density ( $\text{cm}^{-2}$ ) of CN contained in the slab at a depth between  $x_1$  and  $x_2$  after an exposure time  $t$ .

The computed CN column densities of the flight exposed and flight dark control samples versus the thickness are reported in Fig. 10. As expected, the control samples stay along a straight line that passes through the origin. We compute the initial number density of CN as the slope of the linear best fit to the flight dark controls; in particular, we found  $N_{\text{CN}}^0 = 1.94 \times 10^{21}\text{ cm}^{-3}$  that, for a density  $\rho = 1.17\text{ g cm}^{-3}$  (Baratta *et al.*, 2015) of the organic residue, corresponds to an abundance of the CN units of nearly 7% in weight.

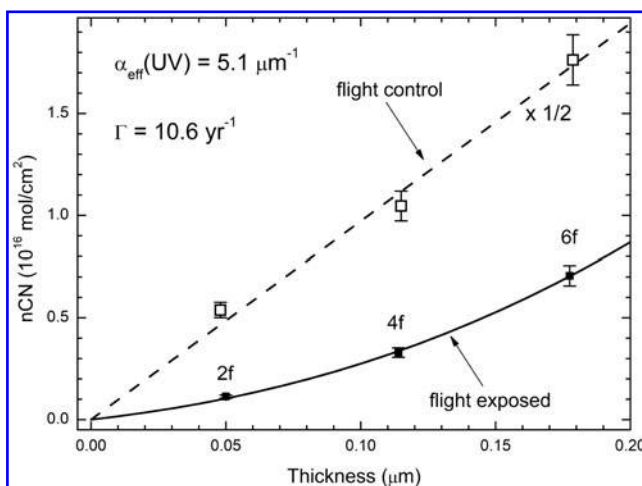


**FIG. 10.** CN column density of the in-flight dark control (open squares) multiplied by a factor of 1/2 and flight exposed (closed squares) samples versus the thickness. The solid curve is the best fit to the flight exposed column density obtained by using Eq. 4. The fit is for 2111 h of solar irradiation at 1 AU. The dashed straight line is the linear best fit to the in-flight dark control column density values.

We use a nonlinear best fit routine, written in IDL language, to fit the column densities of the flight exposed residues with Eq. 4. In Eq. 4, we used the  $N_{\text{CN}}^0$  value determined above and an exposure time  $t$ , over the whole duration of the mission, of 2111 h of equivalent to perpendicular solar irradiation at 1 AU. The equivalent exposure time was provided by RedShift and has been corrected for the transmission losses of the  $\text{MgF}_2$  windows. In Fig. 10, the good agreement between the theoretical fit (solid curve) and the experimental points is evident; the corresponding best fit values of the free parameters  $\alpha(\text{UV})_{\text{eff}}$  and  $\Gamma$  are  $5.1 \mu\text{m}^{-1}$  and  $10.6 \text{yr}^{-1}$ , respectively. If we consider a thin ( $< 50 \text{nm}$ ) organic residue, the lifetime  $\tau$  of the CN units within the film is quite short, in particular  $\tau = \frac{1}{\Gamma} = 0.1$  years. On the other hand, the UV solar flux is exponentially attenuated within the organic residue; hence CN units at greater depths in thicker organic residues can survive much longer times. By using Eq. 4 and the determined  $\alpha(\text{UV})_{\text{eff}}$  and  $\Gamma$  values, we can predict the survival time of the CN units versus the depth at 1 AU. In particular, we compute the CN column density, within a 50 nm thick slab, at variable depth and at different exposure times. The calculated survival curves are reported in Fig. 11. The first curve on the left corresponds to the PSS equivalent to perpendicular solar irradiation exposure, and the solid black circles are the interpolated column densities corresponding to the 2f, 4f, and 6f exposed organic residues. From Fig. 11, it is evident that the CN-bearing species can survive many years in organic residues thicker than  $1 \mu\text{m}$ .

### 3.5. MGR exposed organic residues

In the case of the MGR samples that were irradiated with the solar simulator SOL2000, only wavelengths greater than 200 nm have been used. On the other hand, for EXPOSE-R2 in space, the  $\text{MgF}_2$  windows let photons with wavelength down to 110 nm reach the samples. One of our objectives

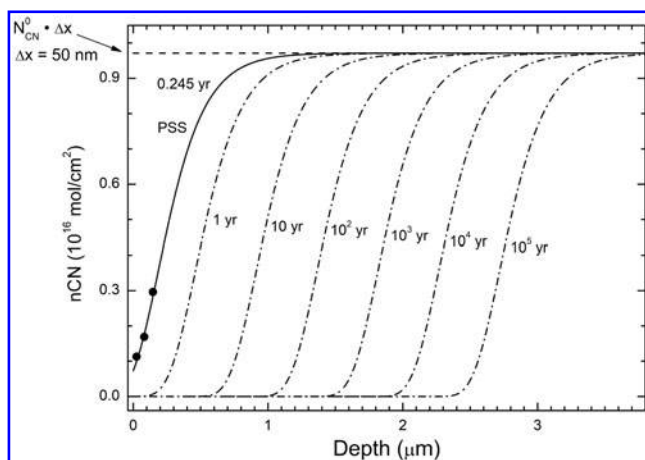


**FIG. 11.** Residual CN column density contained in a 50 nm thick slab at different depths in the organic residue and different exposure time at 1 AU. The horizontal dashed line is the column density value for the unexposed organic residue. The solid line corresponds to the equivalent to perpendicular solar exposure suffered by PSS samples on the ISS. The full circles are the interpolated flight exposed sample data for the three different thicknesses.

was to compare the effects on space exposed samples and ground exposed ones in order to reveal the contribution of the more energetic (below 200 nm) VUV solar photons to modify the samples. Unfortunately, our MGR samples exposed to the solar simulator were contaminated during the ground exposure by a relatively thick film accreted on the  $\text{MgF}_2$  windows from the opposite side to that where the organic residues were deposited and, hence, from the same side of UV exposure. We noted that this contaminant layer was present, with variable amount, on all our MGR samples exposed to the solar simulator but not in any other unexposed MGR sample. From the IR analysis, we know that the contaminant MGR layer spectrum presents a broad strong feature peaking at  $\sim 3450 \text{cm}^{-1}$ , indicating the presence of  $-\text{NH}-$  stretching vibrations (Imanaka *et al.*, 2004). This feature strongly affects the  $3220 \text{cm}^{-1}$  band of the organic residues. Furthermore, since the contaminant layer is on the same side of the incoming UV photons, it interfered with the exposure to the solar simulator. For this reason we decided not to use the spectra of the MGR UV exposed samples for any quantitative comparison with the flight exposed samples. Due to a technical problem, irradiation was not performed under vacuum conditions. In these circumstances, the contamination may have an atmospheric origin. Nevertheless, after cleaning an MGR exposed sample (4f) from the contaminant layer, by polishing the corresponding  $\text{MgF}_2$  window face, we saw that the effects produced by the solar simulator on the IR spectrum were similar, from a qualitative point of view, to the effects seen on the spectrum of the corresponding flight exposed organic residue. This should imply that even less energetic solar UV photons with wavelength greater than 200 nm were effective in modifying the chemical structure of the organic residues.

## 4. Discussion

### 4.1. Solar UV modification of the organic residue

We saw in Section 3.2 that one general effect of the exposure to the UV solar photons is the decreased intensity of the main IR features except for the  $1600 \text{cm}^{-1}$  feature that, in the region between  $1600$  and  $1240 \text{cm}^{-1}$ , gets more intense at low-exposure doses (6f). The reduction in intensity of the features is accompanied by a more or less evident variation of the profile. For the  $3220$  and  $2200 \text{cm}^{-1}$  features, the profile does not change after the initial variation corresponding to the thickest (6f) organic residue. This circumstance seems to indicate that functional groups that give rise to the  $3220 \text{cm}^{-1}$  ( $-\text{NH}_2$ ,  $-\text{NH}-$ , etc.) and  $2200 \text{cm}^{-1}$  ( $-\text{C}\equiv\text{N}$ ,  $-\text{N}\equiv\text{C}$ , etc.) features decrease in number at higher UV exposure without changing their relative amounts. On the other hand, the profile of the  $1600 \text{cm}^{-1}$  feature still changes up to the highest dose (2f sample). In particular, while the peak at  $1590 \text{cm}^{-1}$  decreases more in thinner (higher UV doses) exposed samples (Fig. 6), the wing at lower wavenumbers does not significantly decrease, with respect to the dark control samples, for the three considered thicknesses. Except for the CH bending, according to Ferrari *et al.* (2003),  $\text{C}=\text{C}$  or mixed  $\text{C}=\text{N}$  both in  $\text{sp}^2$  chains and rings is responsible for the broad feature seen in the  $1000$ – $2000 \text{cm}^{-1}$  region for N-rich hydrogenated amorphous carbon nitride (a-C:N:H). We tentatively attribute the initial increased intensity of the wing of the  $1600 \text{cm}^{-1}$  feature to

the possible partial conversion of the  $-\text{C}\equiv\text{N}/-\text{N}\equiv\text{C}$  terminal units lost by the  $2200\text{ cm}^{-1}$  band into  $\text{C}=\text{N}$  units added to the  $\text{C}=\text{C}$  skeleton. Indeed, it is generally found that nitrogen increases the intensity of the  $1600\text{ cm}^{-1}$  feature seen in a-C:N:H (Ferrari *et al.*, 2003). This can be understood if it is taken into account that nitrogen polarizes all the  $\text{sp}^2$  bonds of the conjugated system to which nitrogen is a terminal atom. Thus, it increases the dipole moment of each  $\text{C}=\text{C}$  bond giving rise to an increase in the IR intensity that is larger for longer conjugation. Furthermore, N addition also increases the clustering of the  $\text{sp}^2$  phase, and this also increases the IR intensity. In particular, the integrated absorbance in the  $1000\text{--}1800\text{ cm}^{-1}$  region can be used as an indicator of the N content (Ferrari *et al.*, 2003).

Sharp  $1600\text{--}1580\text{ cm}^{-1}$  peaks are typical of a-C:N:H with high hydrogen content (Ferrari *et al.*, 2003). In particular, these authors observed, in a high H content a-C:N:H film, a sharp peak at  $1580\text{--}1600\text{ cm}^{-1}$  that was as intense as twice the broad wing at  $1300\text{ cm}^{-1}$ . We interpret the decrease of the peak at  $1590\text{ cm}^{-1}$  with respect to the wing at  $1300\text{ cm}^{-1}$ , observed in the flight exposed residues, as due to a progressive loss of hydrogen during solar UV exposure. The loss of hydrogen is also evidenced by the progressive decrease of the broad feature at  $3220\text{ cm}^{-1}$  due to  $-\text{NH}-$ ,  $-\text{NH}_2$ ,  $-\text{CH}_3$ ,  $-\text{CH}_2-$ , and possibly  $-\text{OH}$  functional groups.

Hence, as a consequence of the solar UV exposure, the organic residue is stabilized into a  $\text{C}=\text{C}/\text{C}=\text{N}$  amorphous carbon network, while losing  $-\text{NH}-$ ,  $-\text{NH}_2$  (amine), and  $-\text{C}\equiv\text{N}/-\text{N}\equiv\text{C}$  (nitrile/iso-nitrile) functional groups.

To determine  $\alpha(\text{UV})_{\text{eff}}$  and  $\Gamma$ , we implicitly assumed that the thickness of the flight exposed samples did not change as a consequence of exposure to solar UV photons. On the other hand, we know that the number of functional groups such as amines and nitriles decreased in the flight exposed samples; hence it is plausible that the thickness decreased accordingly if the missing/destroyed species, or some fragments of them, left the UV exposed samples. If we indicate with  $x$  and  $x^{\text{exp}}$  the thickness before and after UV exposure, respectively, in first approximation we can assume that  $x^{\text{exp}} = c \cdot x$ , where the scale factor  $c$  is a constant  $\leq 1$ .

By substituting  $x^{\text{exp}}$  in Eq. 4, the best fit effective absorption coefficient becomes  $\alpha(\text{UV})_{\text{eff}}/c$ , and the destruction rate  $\Gamma$  does not change. Since the effective absorption coefficient would increase ( $c \leq 1$ ), we assume, by continuing to suppose that the thickness after solar UV exposure does not change, a conservative point of view with respect to the nitriles' survival ability at a given depth in the organic residue. Furthermore, although in principle the thickness of the exposed samples could decrease greatly, we observed that the wing of the  $1600\text{ cm}^{-1}$  feature at low wavenumbers does not significantly decrease in the flight exposed samples, with respect to the dark controls, for the three considered thicknesses. In particular, we observe that, due to the solar UV exposure, the organic residue stabilizes into a  $\text{C}=\text{C}/\text{C}=\text{N}$  amorphous carbon network; hence the scaling factor  $c$  is not too far from 1. On the other hand, the scaling factor itself could depend on the sample thickness; nevertheless, the good fit obtained in Fig. 10 should indicate that the scaling factor  $c$  is nearly constant. So far we have implicitly assumed that  $\alpha(\text{UV})_{\text{eff}}$  does not vary as well with the solar UV exposure, and thus it is constant versus the thickness. On the other hand, the conversion of  $-\text{C}\equiv\text{N}$  into  $\text{C}=\text{N}/\text{C}=\text{C}$  units probably

determined an increase of the absorption coefficient in the UV-vis range. Hence, we would expect an increase in the average (versus thickness) absorption coefficient. In this case, the scaling factor  $c$  defined before should decrease with the sample thickness. Nevertheless, we already noted that the scaling factor  $c$  is not too far from 1. Hence, we do not expect a dramatic variation of the absorption coefficient in the range of the UV photons that are effective in destroying the  $-\text{CN}$  units. This confirms the small variation of the absorption coefficient versus the thickness found in the UV range (see Section 3.3). In any case, in addition to the wavelength of the solar UV photons, the  $\alpha(\text{UV})_{\text{eff}}$  coefficient obtained by the fit procedure should be regarded as effective also with respect to the UV exposure. If we suppose, in first approximation, that the absorption coefficient of the preflight organic residue is equal to the absorption coefficient of the organic residue after solar UV exposure, we can obtain some additional information on the wavelength of the solar UV photons that were active in modifying the chemical structure. The absorption coefficient  $\alpha$  is related to the imaginary part of the complex index of refraction  $k$  through the relation  $\alpha = 4\pi k/\lambda$ , where  $\lambda$  is the wavelength. By considering the optical constants of the preflight organic residues given by Baratta *et al.* (2015), and the effective absorption coefficient derived by the best fit procedure  $\alpha(\text{UV})_{\text{eff}} = 5.1\text{ }\mu\text{m}^{-1}$ , we obtain an effective wavelength  $\lambda_{\text{eff}} = 0.342\text{ }\mu\text{m}$ , confirming that less energetic solar UV photons, with wavelength greater than  $200\text{ nm}$ , were effective in modifying the organic residue chemical structure. One could wonder why less energetic UV photons significantly contributed to the destruction of the nitrile units. This can be easily understood if it is noted that the number of absorbed solar UV photons is much larger in the  $200\text{--}400\text{ nm}$  range. In particular, the UV dose absorbed by the organic residue in the  $200\text{--}400\text{ nm}$  range was 390 times larger than the dose absorbed in the  $119.5\text{--}200\text{ nm}$  range (see Section 2.2).

#### 4.2. Survival in the interplanetary medium

Once a comet enters the inner Solar System and the coma develops, a large quantity of dust is lost; it is thought that this dust constitutes a significant fraction of those IDPs that reach Earth's atmosphere (Sandford, 1987).

A major concern regarding the synthesis of biological monomers is the availability of precursor materials under primitive Earth conditions (Ruiz-Mirazo *et al.*, 2014). In this context, two possible sources are commonly considered: endogenous (terrestrial) synthesis and exogenous delivery by comets, meteorites, and IDPs. Among the endogenous processes that could have sown early Earth with suitable precursor materials there are (i) the synthesis of organic aerosols in a neutral or more reducing atmosphere than today (Trainer, 2013; Ferus *et al.*, 2017) or (ii) hydrothermal synthesis (Lemke *et al.*, 2009). The relative amount of organic matter brought by endogenous versus exogenous sources is unknown.

It has been estimated that the delivery of organic carbon (mostly by IDPs, comets, and meteorites) on early Earth was in the order of  $10^8\text{ kg yr}^{-1}$ , or  $10^{16}\text{ kg}$  per 100 million years (Chyba and Sagan, 1992). Since there is about  $6 \times 10^{14}\text{ kg}$  of organic matter in the present biosphere, it is likely that the role of extraterrestrial organics was significant (Ruiz-Mirazo

*et al.*, 2014). Micrometeorites represent the dominant source of extraterrestrial material accreted by Earth today (Taylor, *et al.* 1998). Carbonaceous matter in Antarctic micrometeorites (except UCAMMs) is up to a few percent in weight (Matrajt *et al.*, 2003). UCAMMs are rare. They represent a few percent of the micrometeorites in the CONCORDIA collection. Although UCAMMs have an exceptionally high carbonaceous matter content (from  $\sim 35\%$  to  $\sim 55\%$  in weight; Dobrica *et al.*, 2009), they may not be representative of the majority of the carbonaceous mass delivered to early Earth. Nevertheless, even for very low abundances (a few parts per billion), it is thought that nitriles could be key intermediates to form biologically relevant molecules (Kaiser and Balucani, 2001); indeed, nitriles can be hydrolyzed and react via multistep synthesis ultimately to amino acids.

When not part of an active meteor stream, IDPs spend up to  $10^5$  to  $10^6$  years spiraling toward the Sun (Rietmeijer, 2009). In active meteor streams, the orbital age is shorter but not more than a few millennia (McNaught and Asher, 1999). From Fig. 11, it is evident that a significant fraction of the contained nitriles, provided that there is enough organic residue within the IDPs, has a chance to survive in the interplanetary medium for a long time. Note that, in Fig. 11, we are implicitly assuming that the nitriles present in the unexposed organic residue will be stable for very long periods. From Fig. 5, we are confident that nitriles will be present for many years in residues that are not exposed to UV, but we cannot say whether they continue to be present after  $10^2$  to  $10^3$  years or more. Nevertheless, we already know that a few UCAMMs (Dartois *et al.*, 2013, 2018) have a carbonaceous phase with IR signatures similar to those of the PSS organic residues (Baratta *et al.*, 2015). In particular, these micrometeorites present a  $-\text{C}\equiv\text{N}$  band peaking at around  $2220\text{ cm}^{-1}$  (Dartois *et al.*, 2013, 2018), which is close to the peak position of the nitrile feature observed in the organic residues after solar UV exposure. It is thought that this high organic carbon content (ranging from  $\sim 50\%$  to  $\sim 85\%$  in volume; Dobrica *et al.*, 2009) and high N/C ratio micrometeorites originated in the outer Solar System beyond the nitrogen snow-line, for example in an Oort cloud comet in 100 millions to billions of years by cosmic ray irradiation (Dartois *et al.*, 2013, 2018). Hence, nitriles can survive in UCAMMs for a very long time. On the other hand, according to the results presented in this work, nitriles can be destroyed by exposure to solar UV. In the following, we try to discern the fate of the nitriles contained in an IDP, flying inward from long heliocentric distance, in the hypothesis that the same volume fraction of organic matter present in the UCAMMs previously discussed is made of the PSS organic residue. The objective of this assumption is to take into account, in some way, that in a real IDP other minerals that may have a low absorption efficiency in the UV range are present; this increases the UV field within the IDP with a consequent decrease of the nitriles' lifetime. In the following, we assume that 50% of the IDP volume is occupied by the organic residue, while the remaining 50% is occupied by crystalline forsterite that has a very low absorption coefficient at  $\lambda_{\text{eff}} = 0.342\text{ }\mu\text{m}$ . To describe the absorption, reflection, and refraction of light in the composite material, we use the Maxwell-Garnet effective medium formula. In particular, the effective (average) dielectric

constant of the composite medium  $\epsilon_{\text{av}} = \tilde{N}_{\text{av}}^2$  (where  $\tilde{N}$  is the complex index of refraction) is given by the relation

$$\epsilon_{\text{av}} = \epsilon_{\text{m}} \left[ 1 + \frac{3F_{\text{v}} \frac{\epsilon - \epsilon_{\text{m}}}{\epsilon + 2\epsilon_{\text{m}}}}{1 - F_{\text{v}} \frac{\epsilon - \epsilon_{\text{m}}}{\epsilon + 2\epsilon_{\text{m}}}} \right] \quad (5)$$

where  $\epsilon_{\text{m}}$  is the dielectric constant of the matrix,  $\epsilon$  and  $F_{\text{v}}$  are the dielectric constant and the volume fraction of the inclusions, respectively. We assume that the organic material is the matrix and the inclusions are made of crystalline forsterite in Eq. 5. By considering the absorption coefficient  $\alpha(\text{UV})_{\text{eff}} = 5.1\text{ }\mu\text{m}^{-1}$  and the optical constants of the organic residue (Baratta *et al.*, 2015), we obtain  $\tilde{N}_{\text{m}} = 1.72 - i0.139$  at  $\lambda_{\text{eff}} = 0.342\text{ }\mu\text{m}$ . For crystalline forsterite,  $\tilde{N}(0.342\text{ }\mu\text{m}) = 1.66 - i4 \times 10^{-4}$  (Pitman *et al.*, 2013). At last, by considering a volume fraction  $F_{\text{v}} = 0.5$ , we obtain from Eq. 5  $\tilde{N}_{\text{av}} = 1.69 - i0.069$  at  $\lambda_{\text{eff}} = 0.342\text{ }\mu\text{m}$ . The Maxwell-Garnet formula reported above was derived in the hypothesis of an inhomogeneous medium of a two-component mixture composed of inclusions embedded in an otherwise homogeneous matrix. The inclusions are spherical and small compared with the wavelength. On the other hand, the UCAMMs consist of sub-micrometer-sized minerals embedded in carbonaceous material, where most of the minerals are present in the form of assemblages with sizes in the range from 100 nm up to  $4\text{ }\mu\text{m}$  (Dobrica *et al.*, 2012). Hence, inclusions are not always small compared with the wavelength. Thus, the average complex index of refraction obtained above should be regarded as just an approximation to take into account that the minerals present in the UCAMM may absorb less than the organic material. At any rate, since other minerals found in the UCAMMs may absorb efficiently in the UV (*i.e.*, iron sulfides), the average complex index of refraction obtained by using Eq. 5 should be considered as a conservative estimation.

Here, we consider IDPs of spherical shape and different diameters. We suppose that during their journeys in the interplanetary medium, IDPs assume random orientation with respect to the Sun; hence, the radiation field can be considered isotropic with an intensity that is proportional to  $R^{-2}$  where  $R$  is the heliocentric distance. We consider also IDPs with size significantly larger than the wavelength; hence, in first approximation, geometrical optics can be used to evaluate the field within the particles. In particular, we adopt a ray trace method developed by Liu *et al.* (2002). In this method, the authors derive the internal differential absorption in a sphere of radius  $R_{\text{sph}}$  of complex index of refraction  $\tilde{N} = n - ik$  at a wavelength  $\tilde{\lambda}$ , illuminated by an isotropic field. We indicate with  $F(R_{\text{sph}}, \tilde{N}_{\text{av}}, r)$  the fraction of the incident radiation field transmitted within a sphere of radius  $R_{\text{sph}}$  down to a distance  $r$  from the center. For a sphere Eq. 4 can be modified in:

$$n_{\text{CN}} = \int_0^{R_{\text{sph}}} dN_{\text{CN}} = V_{\text{or}} N_{\text{CN}}^0 4\pi \int_0^{R_{\text{sph}}} e^{-\frac{1}{4}\Gamma \cdot r \cdot F(R_{\text{sph}}, \tilde{N}_{\text{av}}, r)} r^2 dr \quad (6)$$

where the quantity  $F(R_{\text{sph}}, \tilde{N}_{\text{av}}, r)$  is computed by using the ray trace method and  $V_{\text{or}}$  is the volume fraction of the organic residue contained in the IDP. In the hypothesis that the spherical grain is uniformly irradiated, the 1/4 factor in

the exponent takes into account the ratio between the geometrical cross section and the whole surface. At last, the fraction  $F_{\text{CN}}$  of survived  $-\text{C}\equiv\text{N}$  units, within a sphere of radius  $R_{\text{sph}}$  at 1 AU after a time  $t$ , is given by

$$F_{\text{CN}} = \frac{n_{\text{CN}}}{V_{\text{or}} N_{\text{CN}}^0} = \frac{3}{R_{\text{sph}}^3} \int_0^{R_{\text{sph}}} e^{-\frac{1}{4}\Gamma \cdot t \cdot F(R_{\text{sph}}, \bar{N}_{\text{av}}, r)} r^2 dr \quad (7)$$

The resulting survival curves versus the size (diameter) of the IDP are reported in Fig. 12.

The time of flight of an IDP evolving inward (spiraling) under Poynting-Robertson (P-R) drag force from a heliocentric distance  $R$  down to 1 AU is given in the work of Pepin *et al.* (2000):

$$\tau = 1.1 \cdot 10^{14} \delta \rho (R/R_0)^2 \quad (\text{seconds}) \quad (8)$$

where  $\delta$  and  $\rho$  are the diameter and the density of the particle in c.g.s units, respectively,  $R$  is the starting heliocentric distance, and  $R_0$  is the distance that corresponds to 1 AU. Especially for IDPs coming from great heliocentric distances, it should be noted that they spend most of the time far from the Sun and, hence, at much lower UV flux with respect to the flux experienced at 1 AU. Baratta *et al.* (2004) computed the fluence, due to solar wind ions and solar energetic particles, suffered by IDPs under P-R drag force, in the hypothesis that the solar particle flux is proportional to  $R^{-2}$ . In particular, by using Eq. 8, Baratta *et al.* (2004) found that the fluence suffered by an IDP during its P-R drag from a heliocentric distance  $R$  down to 1 AU is the same as that the IDP would suffer at 1 AU in a  $\chi$  times shorter period, where  $\chi = 2 \cdot \ln(R/R_0) \cdot (R/R_0)^{-2}$ . This relation can be used to evaluate the equivalent exposure time to the solar UV photons at 1 AU since the solar photon flux is also proportional to  $R^{-2}$ .

We consider now an IDP flying from a relatively large heliocentric distance  $R = 7$  AU, with a size similar to UCAMM-

D65 ( $\delta = 40 \mu\text{m}$ ) and a density  $\rho = 1 \text{ g cm}^{-3}$ . Using Eq. 8, we obtain  $\tau = 6.8 \cdot 10^5$  years and  $\chi = 7.9 \cdot 10^{-2}$ . Finally, the resulting equivalent exposure time at 1 AU is given by  $\tau\chi = 5.4 \cdot 10^4$  years. From Fig. 12, it is evident that a significant fraction of nitriles can survive within the IDP. As already noted, cometary IDPs that are part of an active meteor stream may have orbital ages as short as a few millennia; in this case, the amount of nitriles that can survive within a  $40 \mu\text{m}$  size IDP would be more than 50%. Nevertheless, even by considering these short exposure periods, nitriles are almost all destroyed in IDPs with sizes smaller than 6–8  $\mu\text{m}$ . If we consider an IDP with a diameter  $\delta = 10 \mu\text{m}$ , flying from 3 AU, we obtain:  $\tau = 3.1 \cdot 10^4$  years,  $\chi = 2.44 \cdot 10^{-1}$  and  $\tau\chi = 7.6 \cdot 10^3$  years. From Fig. 12, we estimate that only 5% of the initial nitriles would survive. There could be some exceptions to the results found so far for relatively small IDPs. In particular, it has been proposed that it is possible to identify dust from comets that formed Earth-crossing dust trails (Messenger, 2002). Unlike the majority of IDPs collected in the stratosphere, which spend millennia or more in space before the Earth encounter, the dust particles may, in this case, have been in space for a few decades or less (Messenger and Walker, 2011). For such “fresh” IDPs, it is evident, from Fig. 12, that a significant fraction of nitriles could have survived even in a  $10 \mu\text{m}$  particle.

It is important to stress that the results reported in Fig. 12 are strictly applicable to an IDP that contains organic matter similar to that of the organic residue studied here. It is of interest to compare the amount of nitriles found in the PSS organic residues with the amount of nitriles found in UCAMMs. We saw that the amount of nitrile units in the PSS organic residues is 7% in weight. We do not have this information for UCAMMs, but we can estimate the relative contribution of the strength of the IR  $-\text{C}\equiv\text{N}$  feature with respect to the  $\text{C}=\text{C}$  feature. In particular, for the UCAMMs studied by Dartois *et al.* (2018), only three of the eight studied present a  $-\text{C}\equiv\text{N}$  IR feature with intensity ratios  $I(-\text{C}\equiv\text{N})/I(\text{C}=\text{C})$  in the range (0.055–0.027). For the PSS flight control organic residue, the intensity ratio is  $I(-\text{C}\equiv\text{N})/I(\text{C}=\text{C}) = 0.18$ , which is 3–7 times higher than that found in UCAMMs. At any rate, provided that the effective absorption coefficient  $\alpha(\text{UV})_{\text{eff}}$  and destruction rate  $\Gamma$  are the same as that found for the PSS organic residues, the survival fraction given by Eq. 7 for an IDP should not depend on the initial amount of nitrile units given by  $V_{\text{or}} N_{\text{CN}}^0$ .

## 5. Conclusion

In the present study, we saw that materials similar to the PSS organic residues could be present on the surface of Solar System objects, such as comets in the Oort cloud, beyond the nitrogen snow-line. When a comet enters into the inner Solar System and the coma develops, a large quantity of dust is lost. This dust constitutes a significant fraction of the IDPs that reach Earth’s atmosphere. Hence, materials similar to that we have produced in laboratory could have reached prebiotic Earth.

According to Ruiz-Mirazo *et al.* (2014), the role of extraterrestrial organics, in providing precursor materials for the synthesis of biological monomers, was significant. Among the organics that could have had a role in providing the bricks from which life could be initiated, there are the nitriles. We know that the nitriles and amines contained in

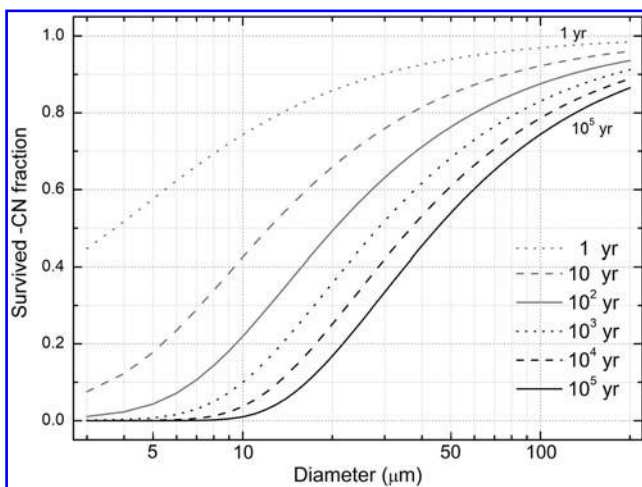


**FIG. 12.** Residual fraction of the CN units contained in spherical IDPs of different radius and different exposure time at 1 AU obtained in the hypothesis that the organic residue is diluted by a factor of 50% in volume and the remaining fraction is made of crystalline forsterite.

some UCAMMs can survive the heating suffered during a present-day atmospheric entry. However, modeling the interaction with the primordial terrestrial atmosphere, to determine the role of UCAMMs as carrier of prebiotic molecules, deserves consideration (Briani *et al.*, 2013).

On the basis of the results obtained on the organic residues exposed outside the ISS, we have shown that the nitriles contained in relatively large IDPs (>20–30  $\mu\text{m}$ ) could have survived in the interplanetary medium; hence they could have reached prebiotic Earth. From Fig. 6, it is evident that the NH amine functional groups appear to be more resistant than nitriles to the solar UV photon irradiation. Hence, it is expected that a significant fraction of amines could also have reached prebiotic Earth. However, we note that UCAMMs represent a few percent of the micrometeorites in the CONCORDIA collection; hence they are probably not representative of the majority of the mass delivered to early Earth. Nevertheless, even for very low abundances (a few parts per billion), nitriles are of particular importance because they are thought to be key intermediates to form amino acids, thus providing one of the basic “ingredients” for life (Kaiser and Balucani, 2001).

### Acknowledgments

This research has been supported by the Italian Space Agency contract n. 2013-073-R.0: PSS (Photochemistry on the Space Station). H.C. acknowledges support by the Centre National d'Etudes Spatiales (CNES). The authors are grateful to E. Li Destri for her help to improve the language of this manuscript.

### Author Disclosure Statement

No competing financial interests exist.

### References

- Accolla, M., Pellegrino, G., Baratta, G.A., Condorelli, G.G., Fedoseev, G., Scirè, C., Palumbo, M.E., and Strazzulla, G. (2018) Combined IR and XPS characterization of organic refractory residues obtained by ion irradiation of simple icy mixtures. *Astron Astrophys* 620, doi:10.1051/0004-6361/201834057.
- Baratta, G.A., Leto, G., and Palumbo, M.E. (2002) A comparison of ion irradiation and UV photolysis of  $\text{CH}_4$  and  $\text{CH}_3\text{OH}$ . *Astron Astrophys* 384:343–349.
- Baratta, G., Mennella, V., Brucato, J.R., Colangeli, L., Leto, G., Palumbo, M.E., and Strazzulla, G. (2004) Raman spectroscopy of ion-irradiated interplanetary carbon dust analogues. *J Raman Spectrosc* 35:487–496.
- Baratta, G.A., Chaput, D., Cottin, H., Fernandez Cascales, L., Palumbo, M.E., and Strazzulla, G. (2015) Organic samples produced by ion bombardment of ices for the EXPOSE-R2 mission on the International Space Station. *Planet Space Sci* 118:211–220.
- Bardyn, A., Baklouti, D., Cottin, H., Fray, N., Briois, C., Paquette, J., Stenzel, O., Engrand, C., Fischer, H., and Hornung, K. (2017) Carbon-rich dust in comet 67P/Churyumov-Gerasimenko measured by COSIMA/Rosetta. *Mon Not R Astron Soc* 469:S712–S722.
- Briani, G., Pace, E., Shore, S.N., Pupillo, G., Passaro, A., and Aiello, S. (2013) Simulations of micrometeoroid interactions with the Earth atmosphere. *Astron Astrophys* 552, doi: 10.1051/0004-6361/201219658.
- Brunetto, R., Barucci, M.A., Dotto, E., and Strazzulla, G. (2006) Ion irradiation of frozen methanol, methane, and benzene: linking to the colors of Centaurs and trans-neptunian objects. *Astrophys J* 644:646–650.
- Chyba, C. and Sagan, C. (1992) Endogenous production, exogenous delivery and impact-shock synthesis of organic molecules: an inventory for the origins of life. *Nature* 355:125–132.
- Ciesla, F.J. and Sandford, S.A. (2012) Organic synthesis via irradiation and warming of ice grains in the solar nebula. *Science* 336:452–454.
- Cooper, J.F., Christian, E.R., Richardson, J.D., and Whang, C. (2003) Proton irradiation of Centaur, Kuiper belt, and Oort cloud objects at plasma to cosmic ray energy. *Earth Moon Planets* 92:261–277.
- Cottin, H., Saiagh, K., Guan, Y.Y., Cloix, M., Khalaf, D., Macari, F., Jérôme, M., Polienor, J.-M., Bénilan, Y., Coll, P., Fray, N., Gazeau, M.-C., Raulin, F., Stalport, F., Carrasco, N., Szopa, C., Bertrand, M., Chabin, A., Westall, F., Vergne, J., Da Silva, L.A., Maurel, M.-C., Chaput, D., Demets, R., and Brack, A. (2015a) The AMINO experiment: a laboratory for astrochemistry and astrobiology on the EXPOSE-R facility of the International Space Station. *Int J Astrobiol* 14:67–77.
- Cottin, H., Saiagh, K., Nguyen, D., Grand, N., Bénilan, Y., Cloix, M., Coll, P., Gazeau, M.-C., Fray, N., Khalaf, D., Raulin, F., Stalport, F., Carrasco, N., Szopa, C., Chaput, D., Bertrand, M., Westall, F., Mattioda, A., Quinn, R., Ricco, A., Santos, O., Baratta, G., Strazzulla, G., Palumbo, M.E., Postollec, A.L., Dobrijevic, M., Coussot, G., Vigier, F., Vandenabeele-Trambouze, O., Incerti, S., and Berger, T. (2015b) Photochemical studies in low Earth orbit for organic compounds related to small bodies, Titan and Mars. Current and future facilities. *Bulletin de la Société Royale des Sciences de Liège* 84:60–73.
- Cottin, H., Kotler, J.M., Billi, D., Cockell, C., Demets, R., Ehrenfreund, P., Elsaesser, A., d'Hendecourt, L., van Loon, J.J.W.A., Martins, Z., Onofri, S., Quinn, R.C., Rabbow, E., Rettberg, P., Ricco, A.J., Slenzka, K., de la Torre, R., de Vera, J.-P., Westall, F., Carrasco, N., Fresneau, A., Kawaguchi, Y., Kebukawa, Y., Dara, N., Poch, O., Saiagh, K., Stalport, F., Yamagishi, A., Yano, H., and Klamm, B.A. (2017) Space as a tool for astrobiology: review and recommendations for experiments in Earth orbit and beyond. *Space Sci Rev* 209: 83–181.
- Dartois, E., Engrand, C., Brunetto, R., Duprat, J., Pino, T., Quirico, E., Remusat, L., Bardin, N., Briani, G., Mostefaoui, S., Morinaud, G., Crane, B., Szwec, N., Delauche, L., Jamme, F., Sandt, Ch., and Dumas, P. (2013) Ultracarbonaceous Antarctic micrometeorites, probing the Solar System beyond the nitrogen snow-line. *Icarus* 224:243–252.
- Dartois, E., Engrand, C., Duprat, J., Godard, M., Charon, E., Delauche, L., Sandt, C., and Borondics, F. (2018) Dome C ultracarbonaceous Antarctic micrometeorites. Infrared and Raman fingerprints. *Astron Astrophys* 609, doi:10.1051/0004-6361/201731322.
- Demets, R., Bertrand, M., Bolkhovitinov, A., Bryson, K., Colas, C., Cottin, H., Dettmann, J., Ehrenfreund, P., Elsaesser, A., Jaramillo, E., Lebert, M., van Papendrecht, G., Pereira, C., Rohr, T., Saiagh, K., and Schuster, M. (2015) Window contamination on EXPOSE-R. *Int J Astrobiol* 14:33–45.
- Demyk, K., Dartois, E., d'Hendecourt, L., Juordain de Muizon, M., Heras, A.M., and Breitfellner, M. (1998) Laboratory identification of the 4.62  $\mu\text{m}$  solid state absorption band in the ISO-SWS spectrum of RAFGL 7009S. *Astron Astrophys* 339: 553–560.

- Dobrica, E., Engrand, C., Duprat, J., Gounelle, M., Leroux, H., Quirico, E., and Rouzaud, J.N. (2009) Connection between micrometeorites and Wild 2 particles: from Antarctic snow to cometary ices. *Meteorit Planet Sci* 44:1643–1661.
- Dobrica, E., Engrand, C., Leroux, H., Rouzaud, J.-N., and Duprat, J. (2012) Transmission Electron Microscopy of CONCORDIA UltraCarbonaceous Antarctic MicroMeteorites (UCAMMs): mineralogical properties. *Geochim Cosmochim Acta* 76:68–82.
- Ferrari, A.C., Rodil, S.E., and Robertson, J. (2003) Interpretation of infrared and Raman spectra of amorphous carbon nitrides. *Phys Rev B* 67, doi:10.1103/PhysRevB.67.155306.
- Ferus, M., Pietrucci, F., Saitta, A.M., Knížek, A., Kubelík, P., Ivanek, O., Shestivska, V., and Civiš, S. (2017) Formation of nucleobases in a Miller–Urey reducing atmosphere. *Proc Natl Acad Sci USA* 114:4306–4311.
- Fray, N., Bardyn, A., Cottin, H., Altwegg, K., Baklouti, D., Briois, C., Colangeli, L., Engrand, C., Fischer, H., Glasmachers, A., Gruen, E., Haerendel, G., Henkel, H., Hoefner, H., Hornung, K., Jessberger, E.K., Koch, A., Kruger, H., Langevin, Y., Lehto, H., Lehto, K., Le Roy, L., Merouane, S., Modica, P., Orthous-Daunay, F.-R., Paquette, J., Raulin, F., Ryno, J., Schulz, R., Silen, J., Siljestrom, S., Steiger, W., Stenzel, O., Stephan, T., Thirkell, L., Thomas, R., Torkar, K., Varnuza, K., Wanczek, K.-P., Zaprudin, B., Kissel, J., and Hilchenbach, M. (2016) High-molecular-weight organic matter in the particles of comet 67P/Churyumov-Gerasimenko. *Nature* 538:72–74.
- Genge, M.J., Engrand, C., Gounelle, M., and Taylor, S. (2008) The classification of micrometeorites. *Meteorit Planet Sci* 43: 497–515.
- Grim, R.J.A. and Greenberg, J.M. (1987) Ions in grain mantles—the 4.62 micron absorption by OCN(-) in W33A. *Astrophys J* 321:L91–L96.
- Grundy, W.M. and Buie, M.W. (2002) Spatial and compositional constraints on non-ice components and H<sub>2</sub>O on Pluto's surface. *Icarus* 157:128–138.
- Guan, Y.Y., Fray, N., Coll, P., Macari, F., Raulin, F., Chaput, D., and Cottin, H. (2010) UVolution: compared photochemistry of prebiotic organic compounds in low Earth orbit and in the laboratory. *Planet Space Sci* 58:1327–1346.
- Heays, A.N., Bosman, A.D., and van Dishoeck, E.F. (2017) Photodissociation and photoionisation of atoms and molecules of astrophysical interest. *Astron Astrophys* 602, doi: 10.1051/0004-6361/201628742.
- Hudson, R.L. and Moore, M.H. (2003) Infrared study of ion-irradiated N<sub>2</sub>-dominated ices relevant to Triton and Pluto: formation of HCN and HNC. *Icarus* 161:486–500.
- Hudson, R.L., Moore, M.H., and Gerakines, P.A. (2001) The formation of cyanate ion (OCN<sup>-</sup>) in interstellar ice analogs. *Astrophys J* 550:1140–1150.
- Hudson, R.L., Moore, M.H., Dworkin, J.P., Mildred, P.M., and Zachary, D.P. (2008) Amino acids from ion-irradiated nitrile-containing ices. *Astrobiology* 8:771–779.
- Imanaka, H., Khare, B.N., Elsila, J.E., Bakes, E.L.O., McKay, C.P., Cruikshank, D.P., Sugita, S., Matsui, T., and Zare, R.N. (2004) Laboratory experiments of Titan tholin formed in cold plasma at various pressures: implications for nitrogen-containing polycyclic aromatic compounds in Titan haze. *Icarus* 168:344–366.
- Kaiser, R.I. and Balucani, N. (2001) The formation of nitriles in hydrocarbon-rich atmospheres of planets and their satellites: laboratory investigations by the crossed molecular beam technique. *Acc Chem Res* 34:699–706.
- Kuzmenko, A.B. (2005) Kramers-Kronig constrained variational analysis of optical spectra. *Rev Sci Instrum* 76, doi: 10.1063/1.1979470.
- Lemke, K.H., Rosenbauer, R.J., and Bird, D.K. (2009) Peptide synthesis in early Earth hydrothermal systems. *Astrobiology* 9:141–146.
- Liu, L.H., Tan, H.P., and Tong, T.W. (2002) Internal distribution of radiation absorption in a semitransparent spherical particle. *J Quant Spectrosc Radiat Transf* 72:747–756.
- Materese, C.K., Cruikshank, D.P., Sandford, S.A., Imanaka, H., Nuevo, M., and White, D.W. (2014) Ice chemistry on outer Solar System bodies: carboxylic acids, nitriles, and urea detected in refractory residues produced from the UV photolysis of N<sub>2</sub>:CH<sub>4</sub>:CO-containing ices. *Astrophys J* 788, doi:10.1088/0004-637X/788/2/111.
- Matrajt, G., Taylor, S., Flynn, G., Brownlee, D.E., and Joswiak, D. (2003) A nuclear microprobe study of the distribution and concentration of carbon and nitrogen in Murchison and Tagish Lake meteorites, Antarctic micrometeorites, and IDPs: implications for astrobiology. *Meteorit Planet Sci* 38: 1585–1600.
- McNaught, R.H. and Asher, D.J. (1999) Leonid dust trails and meteor storms. *WGN, Journal of the International Meteor Organization* 27:85–102.
- Messenger, S. (2000) Identification of molecular-cloud material in interplanetary dust particles. *Nature* 404:968–971.
- Messenger, S. (2002) Opportunities for the stratospheric collection of dust from short-period comets. *Meteorit Planet Sci* 37:1491–1505.
- Messenger, S. and Walker, R.M. (2011) Stratospheric collection of dust from comet 73P/Schwassmann-Wachmann 3 [abstract 2158]. In *42<sup>nd</sup> Lunar and Planetary Science Conference*, Lunar and Planetary Institute, Houston.
- Mutsukura, N. and Akita, K. (1999) Infrared absorption spectroscopy measurements of amorphous CN<sub>x</sub> films prepared in CH<sub>4</sub>/N<sub>2</sub> r.f. discharge. *Thin Solid Films* 349:115–119.
- Onofri, S., Barreca, D., Selbmann, L., Isola, D., Rabbow, E., Horneck, G., de Vera, J.P.P., Hatton, J., and Zucconi, L. (2008) Resistance of Antarctic black fungi and cryptoendolithic communities to simulated space and martian conditions. *Stud Mycol* 61:99–109.
- Palumbo, M.E., Strazzulla, G., Pendleton, Y.J., and Tielens, A.G.G.M. (2000a) ROCN species produced by ion irradiation of ice mixtures: comparison with astronomical observations. *Astrophys J* 534:801–808.
- Palumbo, M.E., Pendleton, Y.J., and Strazzulla, G. (2000b) Hydrogen isotopic substitution studies of the 2165 wavenumber (4.62 micron) “XCN” feature produced by ion bombardment. *Astrophys J* 542:890–893.
- Palumbo, M.E., Ferini, G., and Baratta, G.A. (2004) Infrared and Raman spectroscopies of refractory residues left over after ion irradiation of nitrogen-bearing icy mixtures. *Adv Space Res* 33:49–56.
- Palumbo, M.E., Leto, P., Siringo, C., and Trigilio, C. (2008) Detection of C<sub>3</sub>O in the low-mass protostar Elias 18. *Astrophys J* 685:1033–1038.
- Pendleton, Y.J. and Allamandola, L.J. (2002) The organic refractory material in the diffuse interstellar medium: mid-infrared spectroscopic constraints. *Astrophys J* 138:75–98.
- Pepin, R.O., Palma, R.L., and Schlutter, D.J. (2000) Noble gases in interplanetary dust particles, I: The excess helium-3 problem and estimates of the relative fluxes of solar wind and solar energetic particles in interplanetary space. *Meteorit Planet Sci* 35:495–504.

- Pitman, K.M., Hofmeister, A.M., and Speck, A.K. (2013) Revisiting astronomical crystalline forsterite in the UV to near-IR. *Earth Planets Space* 65:129–138.
- Protopapa, S., Grundy, W.M., Reuter, D.C., Hamilton, D.P., Dalle Ore, C.M., Cook, J.C., Cruikshank, D.P., Schmitt, B., Philippe, S., Quirico, E., Binzel, R.P., Earler, A.M., Ennico, K., Howett, C.H.A., Lunsford, A.W., Olkin, C.B., Parker, A., Singer, K.N., Stem, A., Verbiscer, A.J., Weaver, H.A., Young, L.A., the New Horizons Science Team. (2017) Pluto's global surface composition through pixel-by-pixel Hapke modeling of New Horizons Ralph/LEISA data. *Icarus* 287:218–228.
- Quirico, E., Montagnac, G., Lees, V., McMillan, P.F., Szopad, C., Cernogora, G., Rouzaud, J., Simon, P., Bernard, J., Coll, P., Frayh, N., Minardi, R.D., Raulin, F., Reynard, B., and Schmitt, B. (2008) New experimental constraints on the composition and structure of tholins. *Icarus* 198:218–231.
- Rabbow, E., Rettberg, P., Parpart, A., Panitz, C., Schulte, W., Molter, F., Jaramillo, E., Demets, R., Weiß, P., and Willnecker, R. (2017) EXPOSE-R2: the astrobiological ESA mission on board of the International Space Station. *Front Microbiol* 8, doi:10.3389/fmicb.2017.01533.
- Rietmeijer, F. (2009) A cometary aggregate interplanetary dust particle as an analog for comet Wild 2 grain chemistry preserved in silica-rich Stardust glass. *Meteorit Planet Sci* 44: 1589–1609.
- Ruiz-Mirazo, K., Briones, C., and de la Escosura, A. (2014) Prebiotic systems chemistry: new perspectives for the origins of life. *Chem Rev* 114:285–366.
- Sandford, S.A. (1987) The collection and analysis of extraterrestrial dust particles. *Fundamentals of Cosmic Physics* 12:1–73.
- Sandford, S.A., Messenger, S., DiSanti, M., Keller, L., and Altwegg, K. (2008) Oxygen in comets and interplanetary dust particles. *Reviews in Mineralogy and Geochemistry* 68:247–272.
- Sicilia, D., Ioppolo, S., Vindigni, T., Baratta, G.A., and Palumbo, M.E. (2012) Nitrogen oxides and carbon chain oxides formed after ion irradiation of CO:N<sub>2</sub> ice mixtures. *Astron Astrophys* 543, doi:10.1051/0004-6361/201219390.
- Stern, S.A. (2003) The evolution of comets in the Oort cloud and Kuiper belt. *Nature* 424:639–642.
- Strazzulla, G. and Johnson, R.E. (1991) Irradiation effects on comets and cometary debris. In *Comets in the Post-Halley Era*, Vol. 1, ASSL Series, Springer, Dordrecht, pp 243–275.
- Strazzulla, G., Cooper, J.F., Christian, E.R., and Johnson, R.J. (2003) Irradiation ionique des OTNs: des flux mesurés dans l'espace aux expériences de laboratoire. *Comptes Rendus Physic* 4:791–801.
- Szabó, Gy.M., Sárneczky, K., and Kiss, L.L. (2011) Frozen to death? Detection of comet Hale-Bopp at 30.7 AU. *Astron Astrophys* 531, doi:10.1051/0004-6361/201116793.
- Taylor, S., Lever, J.H., and Harvey, R.P. (1998) Accretion rate of cosmic spherules measured at the South Pole. *Nature* 392: 899–903.
- Trainer, M.G. (2013) Atmospheric prebiotic chemistry and organic hazes. *Curr Org Chem* 17:1710–1723.
- Urso, R., Scirè, C., Baratta, G.A., Compagnini, G., and Palumbo, M.E. (2016) Combined infrared and Raman study of solid CO. *Astron Astrophys* 594, doi:10.1051/0004-6361/201629030.
- Ziegler, J.F., Ziegler, M.D., and Biersack, J.P. (2008) *The Stopping and Range of Ions in Solids*, Pergamon Press, New York. Available online at <http://www.srim.org>

Address correspondence to:

G.A. Baratta  
 INAF - Osservatorio Astrofisico di Catania  
 via Santa Sofia 78  
 95123 Catania  
 Italy

E-mail: gbaratta@oact.inaf.it

Submitted 7 March 2018

Accepted 15 November 2018

#### Abbreviations Used

|   |
|---|
| DLR = German Aerospace Center (Deutsches Zentrum für Luft- und Raumfahrt) |
| EVA = extravehicular activity   |
| FTIR = Fourier-transform infrared   |
| GCR = galactic cosmic ray   |
| IDP = interplanetary dust particle  |
| ISS = International Space Station   |
| MGR = Mission Ground Reference  |
| P-R = Poynting-Robertson  |
| PSS = Photochemistry on the Space Station                                 |
| TNOs = trans-neptunian objects  |
| UCAMMs = ultracarbonaceous Antarctic micrometeorites                      |
| UHV = ultrahigh vacuum  |
| VUV = vacuum UV   |

**This article has been cited by:**

1. Cottin Hervé, Rettberg Petra. 2019. EXPOSE-R2 on the International Space Station (2014–2016): Results from the PSS and BOSS Astrobiology Experiments. *Astrobiology* **19**:8, 975–978. [[Abstract](#)] [[Full Text](#)] [[PDF](#)] [[PDF Plus](#)]